



Contents lists available at ScienceDirect

Thin Solid Films

journal homepage: [www.elsevier.com/locate/tsf](http://www.elsevier.com/locate/tsf)

## Simulating the opto-thermal processes involved in laser induced self-assembly of surface and sub-surface plasmonic nano-structuring

D.V. Bellas<sup>a</sup>, D. Toliopoulos<sup>a</sup>, N. Kalfagiannis<sup>b</sup>, A. Siozios<sup>a</sup>, P. Nikolaou<sup>c</sup>, P.C. Kelires<sup>c</sup>, D.C. Koutsogeorgis<sup>b</sup>, P. Patsalas<sup>d</sup>, E. Lidorikis<sup>a,\*</sup>

<sup>a</sup> Department of Materials Science and Engineering, University of Ioannina, GR-45110 Ioannina, Greece

<sup>b</sup> School of Science and Technology, Nottingham Trent University, NG11 8NS Nottingham, United Kingdom

<sup>c</sup> Research Unit for Nanostructured Materials Systems, Department of Mechanical Engineering and Materials Science Engineering, Cyprus University of Technology, P.O. Box 50329, 3603 Limassol, Cyprus

<sup>d</sup> Department of Physics, Aristotle University of Thessaloniki, GR-54124 Thessaloniki, Greece

### ARTICLE INFO

#### Article history:

Received 17 June 2016

Received in revised form 22 November 2016

Accepted 23 December 2016

Available online xxx

#### Keywords:

Plasmonics

Laser annealing

Nanostructure

Nanophotonics

Nanopatterning

Optothermal

Plasmonic writing

### ABSTRACT

Nano-structuring of metals is one of the greatest challenges for the future of plasmonic and photonic devices. Such a technology calls for the development of ultra-fast, high-throughput and low cost fabrication techniques. Laser processing accounts for the aforementioned properties, representing an unrivalled tool towards the anticipated arrival of modules based in metallic nano-structures, with an extra advantage: the ease of scalability. Specifically, laser nano-structuring of an ultra-thin metal film or an alternating metal film on a substrate/metal film on a substrate results respectively on surface (metallic nanoparticles on the surface of the substrate) or subsurface (metallic nanoparticles embedded in a dielectric matrix) plasmonic patterns with many applications. In this work we investigate theoretically the photo-thermal processes involved in surface and sub-surface plasmonic nano-structuring and compare to experiments. To this end, we present a design process and develop functional plasmonic nano-structures with pre-determined morphology by tuning the annealing parameters like the laser fluence and wavelength and/or the structure parameters like the thickness of the metallic film and the volume ratio of the metal film on a substrate-metal composite. For the surface plasmonic nano-structuring we utilize the ability to tune the laser's wavelength to either match the absorption spectral profile of the metal or to be resonant with the plasma oscillation frequency, i.e. we utilize different optical absorption mechanisms that are size-selective. Thus, we overcome a great challenge of laser induced self assembly by combining simultaneously large-scale character with nanometer scale precision. For subsurface plasmonic nano-structuring, on the other hand, we utilize the temperature gradients that are developed spatially across the metal/dielectric nano-composite structure during the laser treatment. We find that the developed temperature gradients are strongly dependent on the nanocrystalline character of the dielectric host which determines its thermal conductivity, the composition of the ceramic/metal and the total thickness of the nano-composite film. The aforementioned material parameters combined with the laser annealing parameters can be used to pre-design the final morphology of the sub-surface plasmonic structure. The proposed processes can serve as a platform that will stimulate further progress towards the engineering of plasmonic devices.

© 2017 The Authors. Published by Elsevier B.V. This is an open access article under the CC BY-NC-ND license (<http://creativecommons.org/licenses/by-nc-nd/4.0/>).

### 1. Introduction

Plasmonic nanoparticles (NPs) are metallic nanoparticles with sizes much smaller than the wavelength of visible light. When plasmonic NPs are irradiated by electromagnetic waves their free electrons oscillate as a response to the external electric field. At the appropriate frequency the oscillation becomes resonant with extreme optical response; this optical phenomenon is known as Localized Surface Plasmon Resonance (LSPR) [1–10]. This strong light/electron coupling forces the

confinement of light into small volumes and results into extreme local fields, light scattering and absorption [11–13]. The LSPR phenomenon induced in NPs depends strongly on their composition, size, shape, geometrical distribution and on the refractive index of the employed dielectric environment [14–19]. In this regard, efforts are undertaken in order to control these structural parameters depending on the growth conditions [5,6,20–23]. Noble metals gold and silver are considered more suitable for NPs due to their stability when formed into nanoparticles and their strong LSPR absorption bands in the visible region of the spectrum [12,21]. The LSPR is an enabling optical phenomenon for a number of exciting applications including biochemical sensing [24–27], surface enhanced spectroscopies [11,28–34], information and communication

\* Corresponding author.

E-mail address: [elidorik@cc.uoi.gr](mailto:elidorik@cc.uoi.gr) (E. Lidorikis).

technologies [35–38], solar energy harvesting [39–46], optical encoding [47–50], surface decoration [51], lighting [52] and many others. In particular, we have recently shown that plasmonic nanocomposites consisting of silver nanoparticles, with sizes ranging from 3 to 200 nm, embedded into either ceramic [47–50] or polymer [44] dielectric matrices can be effective templates for overt [49] or covert [50] spectrally-selective optical patterns and graded solar photothermal absorbers [44].

A critical parameter in delivering the aforementioned devices is the material preparation method, which should allow for the production of nanostructures with tunable plasmonic properties. So far, nanomaterial and nanodevice manufacturing has traditionally followed two distinct routes: a) the top-down approach, a process that starts from a uniform material and subsequently uses finer and finer tools for creating correspondingly smaller structures, like lithographic processes [53–55] and/or ion beam nanofabrication [56], and b) the bottom-up approach, where smaller components of atomic or molecular dimensions self-assemble together, according to a natural physical principle or an externally applied driving force, to give rise to larger and more organized systems, like atomic layer deposition [57], cold welding [58], flash thermal annealing [48,59,60], pattern transfer [61] and template stripping [62–64]. In practice, the top-down route offers unparalleled control and reproducibility down to a few nanometers in feature size but at high cost for a large area processing, while the bottom-up approach naturally applies for macroscopic scale nano-patterning albeit without the fine feature and reproducibility control.

The use of laser radiation is an intermediate route for nanotechnology. Light-matter interactions offer precise energy delivery and control over the physico-chemical processes in the nanoworld. Amongst the methodologies followed for creating nanoparticle arrangements and/or nano-composite thin films, Laser Annealing (LA) has been proven to be simple and versatile, providing freedom of design, fast processing, compatibility with large scale manufacturing and allowing for the use of inexpensive flexible substrates [47,49,65]. For example, LA of a thin metal film results into nanoparticle arrangements on top of the substrate [31,34,65–77], while embedded plasmonic NPs in a dielectric matrix can be fabricated in large scale by the LA of a stack of alternating ultrathin layers of metal and dielectric [47,48]. It is noteworthy that the actual visual appearance of a plasmonic nanocomposite would be affected exclusively by the electron scattering in silver and the refractive index of the matrix, independently of the rest of its structural features (such as the crystallinity and the chemical composition) and functional properties (such as the thermal conductivity and the mechanical properties). For example, Fig. 1 shows two plasmonic nanocomposites consisting of Ag nanoparticles embedded into a ceramic (AlN) or a polymer (PDMS) matrix, which have similar appearance but the rest of their properties are completely different. Therefore plasmonic nanocomposites might share similar interactions with light while their thermal and mechanical responses would be exceptionally varying during laser processing, as we will discuss below.

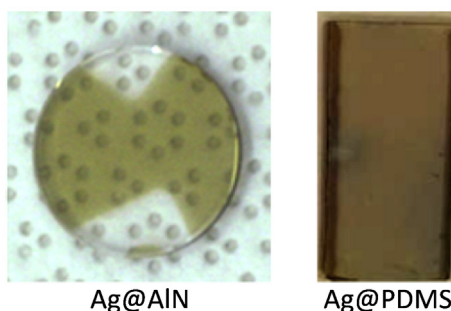


Fig. 1. Images of two samples of plasmonic nanocomposites with a ceramic AlN [48] or polymer PDMS [44] matrix.

One of the key theoretical/design issues in LA is the spatial distribution of the energy delivered from the laser pulse and the precise temporal temperature profile created in the structure due this to energy. Knowing how the temperature profiles depend on the nanoparticle/substrate geometries will give us valuable insight so to be able to tailor-design the LA process and get custom-made plasmonic devices. In the systems of interest, several effects such as material absorption, plasmon resonances and interference contribute to how the absorption is distributed, while the material thermal properties and the laser pulse profile determine the temperature transients developed. Here, we present the theoretical investigations required in order to extract the underline physical understanding of all these photo-thermal processes involved in surface and sub-surface laser nano-structuring, and propose ways to experimentally develop plasmonic nano-structures with pre-determined morphology. We then illustrate that theory and experiments are in good agreement and thus prove that theory can indeed be a valuable tool in assisting and driving the development of functional plasmonic nano-structures. We focus on two specific examples, the first one involving the subsurface nanostructuring of a metal/ceramic multilayer film by a single laser shot, while the second one involving the fine tuning of the surface morphology of a single metallic film by multiple pulse irradiation.

For the sub-surface plasmonic nanostructuring, we first develop an analytical model which calculates the light propagation properties and obtain a detailed spatial absorption distribution in the multilayer and the substrate. Furthermore we compare the analytical absorption distribution with the numerical one extracted from Finite-Difference Time-Domain (FDTD) calculations and we find excellent agreement. This spatial distribution is then integrated with the experimental laser temporal profile and solved in a 1D heat transport equation, arriving at the temperature transients at each point in the multilayer volume. We perform this analysis for different structure parameters like metal/ceramic volume ratio, thickness of the multilayer and thermal conductivity of the dielectric ceramic matrix. We find that significant temperature gradients are developed spatially across the nano-composite structure, which strongly depend on the aforementioned material parameters. Furthermore, presenting the experimental results we show that these temperature gradients create different annealing conditions across the nano-composite structure and can be used to design the final morphology of the plasmonic structure.

For the surface plasmonic nanostructuring, we first simulate the UV and optical light absorption for different silver nanoparticle sizes and arrangements on top of a Si substrate and thus we get the spatial absorption profile. For the UV and optical calculations a full vector 3D FDTD simulator is used in order to capture the possible absorption mechanisms that are size selective and enable geometric specificity: a) interband absorption, resulting from the excitation of the metal's internal  $d$ -electrons into the conduction band and b) intraband absorption, resulting from the metal's free electrons resonantly excited at the specific spectral position of the LSPR. Utilizing the absorption spatial profile, we then perform heat diffusion simulations taking into account the exact laser temporal pulse profile and arrive at the transient temperature profile in each nanoparticle. From this we map the maximum temperature rise as a function of particle size, laser wavelength and laser fluence. In these maps we distinguish spectral regions of higher and lower temperature which can be used to provide a recipe for the modification of the plasmonic templates towards a predefined morphology. In particular, by sequentially tuning the laser wavelength into resonance with different physical processes such as the LSPR of the metal particles or the interband transitions of the metal's  $d$ -electrons, we can selectively target the melting and re-solidification of different particle size groups. This idea is implemented in experiments, in which repeated laser treatments target different NPs size groups with different laser wavelengths, driving the final size distribution towards the predetermined one. We term this process: “Modification of Nanoparticle Arrays by Laser Induced Self Assembly” (MONA-LISA).

2. Subsurface nano-structuring

2.1. Theoretical approach

Our model system consists of a stratified multilayer structure of alternating dielectric (AlN) and metal layers (Ag) on a Si substrate (Fig. 2). The optical response of such multilayer shows high UV absorption (Fig. 2a) due to silver's interband transitions at this spectral range. Interestingly, absorption is higher at lower Ag volume ratio because of the lower reflection losses. Under the proper experimental conditions, this high UV absorption is utilized to locally melt the structure. Due to the immiscibility of Ag with AlN, Ag diffusion will drive its transformation into a plasmonic nano-composite with metallic NPs embedded in a dielectric matrix (Fig. 2b). The morphology of the nano-composite and its optical response can be tuned by choosing materials and laser annealing parameters such as: the nanocrystalline character of the dielectric which is strongly related to its thermal conductivity, the metal volume ratio and the total thickness of the multilayer. Our modeling sheds light on the contribution of each one of the above parameters to the temperature profiles created, and thus to the final structure.

First, we start with the UV optical constants of the metal and dielectric and develop an analytical model which provides the absorption spatial distribution in the multilayer. We assume an array of AlN/Ag bilayers on top of a Si substrate, as shown in Fig. 3a, where  $l_{AlN}$ ,  $\tilde{\epsilon}_{AlN}$ ,  $l_{Ag}$ ,  $\tilde{\epsilon}_{Ag}$  are the thickness and the complex dielectric function of AlN and Ag respectively. The thickness of the Si is semi-infinite and  $\tilde{\epsilon}_{Si}$  is the dielectric function of Si. The volume ratio of Ag is  $f_{Ag} = l_{Ag} / (l_{AlN} + l_{Ag})$ . The optical constants are obtained from optical ellipsometric measurements for Ag [78] and for AlN [79]. If the individual layers are much smaller than the laser wavelength (a necessary condition in order to end up with subwavelength composites), we can assume the effective medium dielectric function by volume-averaging the individual experimental dielectric functions of Ag and AlN [80–82]:  $\tilde{\epsilon}_{eff} = f_{AlN}\tilde{\epsilon}_{AlN} + f_{Ag}\tilde{\epsilon}_{Ag}$  and the effective refractive index  $\tilde{n}_{eff} = \sqrt{\tilde{\epsilon}_{eff}} = n_{eff} + ik_{eff}$  where  $n_{eff}$ ,  $k_{eff}$  is the real and imaginary part of the complex refractive index respectively. Utilizing the effective medium optical constants we can now model a uniform film which has the same thickness and optical response as that of the multilayer (Fig. 3b), but is now amenable to a simple analytical treatment to extract the absorption spatial distribution in the film and substrate under UV illumination. Specifically, as it is shown in Fig. 3b, under illumination a portion of light is reflected (reflection amplitude  $r$ ) and the rest undergoes multiple reflections from the air/film and film/Si interfaces and gets absorbed along the way. The resulting coherent downward and upward waves are denoted by  $A(x)$  and  $B(x)$  respectively. The transmitted wave is denoted by  $C$ , with  $C(x_s)$  the wave at a specific distance  $x_s$  from the Si-film interface. Practically,  $C(x_s)$  diminishes within the first 100 nm due to high absorbance of Si in the UV region.

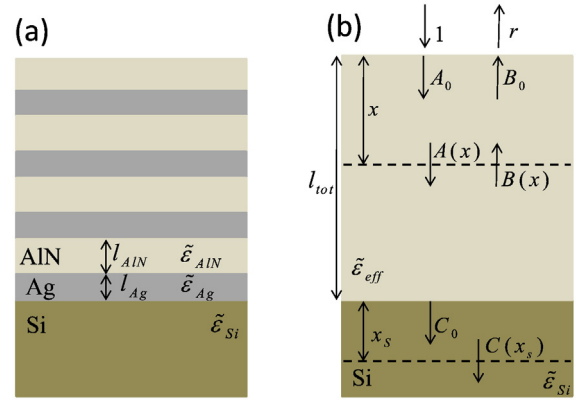


Fig. 3. Schematic of the multilayer structure a) the stratified AlN/Ag multilayer structure and b) the effective composite structure illustrating the analytical model.

We first calculate the incident and transmitted waves from the effective film, through transfer matrixes:

$$\begin{pmatrix} C_0 \\ 0 \end{pmatrix} = I_{\tilde{n}_{Si}\tilde{n}_f} P_{\tilde{n}_f l_{tot}} I_{\tilde{n}_f n_a} \begin{pmatrix} 1 \\ r \end{pmatrix} = \begin{pmatrix} M_{11} & M_{12} \\ M_{21} & M_{22} \end{pmatrix} \begin{pmatrix} 1 \\ r \end{pmatrix} \quad (1)$$

where  $I_{\tilde{n}_f n_a}$  is the interface matrix from air to the film,  $P_{\tilde{n}_f l_{tot}}$  is the propagation matrix in the film and  $I_{\tilde{n}_{Si}\tilde{n}_f}$  is the interface matrix from film to Si substrate:

$$\begin{aligned} I_{\tilde{n}_f n_a} &= \frac{1}{2\tilde{n}_f} \begin{pmatrix} \tilde{n}_f + n_a & \tilde{n}_f - n_a \\ \tilde{n}_f - n_a & \tilde{n}_f + n_a \end{pmatrix} \\ P_{\tilde{n}_f l_{tot}} &= \begin{pmatrix} e^{ik_f l_{tot}} & 0 \\ 0 & e^{-ik_f l_{tot}} \end{pmatrix} \\ I_{\tilde{n}_{Si}\tilde{n}_f} &= \frac{1}{2\tilde{n}_{Si}} \begin{pmatrix} \tilde{n}_{Si} + \tilde{n}_f & \tilde{n}_{Si} - \tilde{n}_f \\ \tilde{n}_{Si} - \tilde{n}_f & \tilde{n}_{Si} + \tilde{n}_f \end{pmatrix} \end{aligned} \quad (2)$$

where  $n_a$ ,  $\tilde{n}_f \equiv \tilde{n}_{eff}$ ,  $\tilde{n}_{Si}$  are the refractive indexes of the air, the effective index of the film and the refractive index of the Si substrate respectively. From Eqs. (1) and (2) we derive the complex components of the transfer matrix  $M$ :

$$\begin{aligned} M_{11} &= \frac{1}{2} \left( 1 + \frac{n_a}{\tilde{n}_{Si}} \right) \cos(k_f l_{tot}) + \frac{i}{2} \left( \frac{n_a}{\tilde{n}_f} + \frac{\tilde{n}_f}{\tilde{n}_{Si}} \right) \sin(k_f l_{tot}) \\ M_{21} &= \frac{1}{2} \left( 1 - \frac{n_a}{\tilde{n}_{Si}} \right) \cos(k_f l_{tot}) + \frac{i}{2} \left( \frac{n_a}{\tilde{n}_f} - \frac{\tilde{n}_f}{\tilde{n}_{Si}} \right) \sin(k_f l_{tot}) \end{aligned} \quad (3)$$

where  $k_f = 2\pi\tilde{n}_f/\lambda$  is the wave vector inside the film. The other two components are the respective complex conjugates, i.e.  $M_{12} = M_{21}^*$  and  $M_{22} = M_{11}^*$ . Combining Eqs. (1) and (3) we get the reflected  $r = -M_{21}/M_{22}$  and transmitted  $C_0 = \det(M)/M_{22}$  waves. Focusing

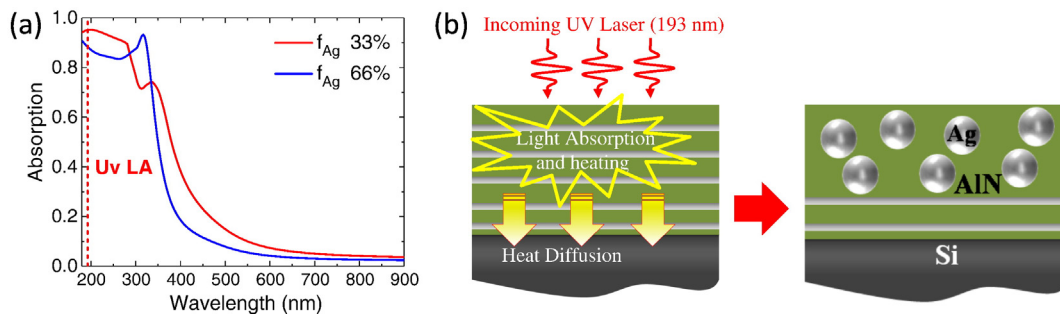


Fig. 2. a) Spectral absorption of a stratified metal (Ag) dielectric (AlN) structure illustrated in (b) for two metal volume ratios 33% and 66%. The high UV absorption can be utilized for the further modification of the nano-composite. b) Schematic illustration of the laser treatment of the multilayer structure. Under UV laser radiation, the absorbed energy is converted into heat which diffuses by thermal conduction into the Si substrate. The result of the laser treatment is to transform the multilayer structure into a nano-composite of embedded plasmonic metallic NPs inside a dielectric matrix.

next on the air-film interface we associate the waves before the interface with the waves after the interface:

$$\begin{pmatrix} A_0 \\ B_0 \end{pmatrix} = I_{\tilde{n}_f n_a} \begin{pmatrix} 1 \\ r \end{pmatrix} = \begin{pmatrix} N_{11} & N_{12} \\ N_{21} & N_{22} \end{pmatrix} \begin{pmatrix} 1 \\ r \end{pmatrix} \quad (4)$$

The fields after the air-film interface thus are:

$$A_0 = \frac{N_{11}M_{22} - N_{12}M_{21}}{M_{22}} \quad (5)$$

$$B_0 = \frac{N_{21}M_{22} - N_{22}M_{21}}{M_{22}}$$

These waves are counter propagating in the film and at a distance  $x$  from the interface they are  $A(x) = A_0 e^{ik_f x}$  and  $B(x) = B_0 e^{-ik_f x}$ , both waves decreasing exponentially with distance along the propagation direction ( $+x$  for the forward wave,  $-x$  for the backward wave). Also the wave propagating in the semi-infinite silicon substrate is described as  $C(x_s) = C_0 e^{ik_s x_s}$ , where  $x_s$  is the distance from the film-Si interface and  $k_s = 2\pi\tilde{n}_s/\lambda$  is the wave vector in the Si substrate. We can calculate the Poynting vector  $S$  at each point in the film and in the Si substrate [83]:

$$S(x) = \text{Re}\{\tilde{n}_f\} (|A(x)|^2 - |B(x)|^2) - 2\text{Im}\{\tilde{n}_f\} \text{Im}\{A(x)B^*(x)\} \quad (6)$$

$$S(x_s) = \text{Re}\{\tilde{n}_f\} |C(x_s)|^2 \quad (7)$$

The first term in Eq. (6) is associated with the forward  $A(x)$  and backward  $B(x)$  waves, as if each of them was propagating independent of each other. The second term, which is absent in the case of non-absorbing media, appears here because of the interference between the counter-propagating waves in the absorbing film. To get the detailed absorption profile, we calculate the absorption per nm from the top of the film down to the Si substrate:

$$A(x) = S(x) - S(x-1) \quad (8)$$

where  $x$  is measured in nm.

To validate our analytic effective medium approach, we also perform computational simulations for the light propagation, thus we obtain numerically the absorption spatial distribution and compare it with the analytically one extracted from the above model. In our numerical simulations we time-integrate Maxwell's equations [84] on a computational grid and solve for the light propagation utilizing the FDTD method [85]. We use an in-house 3D FDTD simulator [86–88] which is able to handle all possible designed geometries and different materials. Material dispersion is introduced in the form of polarization equations coupled and solved concurrently with Maxwell's equations, where the various parameters defining the optical constants of the materials are obtained by performing a Drude-Lorentz fit to the experimental dielectric function obtained from ellipsometric measurements [86–88]. This process effectively takes into account both intraband and interband transitions.

For the FDTD simulations, we assume two multilayer structures with different volume ratios of silver, one with  $f_{Ag} = 33\%$  (20 repetitions of 4 nm-AlN/2 nm-Ag bilayers on Si substrate, with a total multilayer thickness  $l_{tot} = 120$  nm) and one with  $f_{Ag} = 66\%$  (20 repetitions of 2 nm-AlN/4 nm-Ag bilayers on Si substrate, total multilayer thickness  $l_{tot} = 120$  nm), described by the thickness and dielectric functions of the individual layers, and obtain a detailed map of the UV ( $\lambda = 193$  nm) absorption spatial distribution. Comparing numerical and analytical absorption spatial profiles for the two silver volume ratios we find perfect agreement as it is illustrated in Fig. 4a and b. From now on we use the analytical effective medium model to obtain the absorption spatial distribution in the multilayer and Si substrate.

The obtained absorption spatial distribution  $a()$  combined with the experimental laser pulse profile  $\phi(t)$  (Fig. 4c) are used as the laser

induced heating source  $Q(x, t) = a(x) \cdot \phi(t)$  and solved numerically in the 1D heat diffusion equation:

$$(c\rho)_{eff}(x) \frac{\partial T(xt)}{\partial t} = \frac{\partial}{\partial x} \left[ k_{eff}(T(xt)) \frac{\partial T(xt)}{\partial x} \right] + Q(xt) \quad (9)$$

where  $T$  is the local temperature transient and the material parameters mass density  $\rho$ , heat capacity  $c$ , thermal conductivity  $k$  are in general both space and temperature dependent. The total laser fluence is  $f = \int_{-\infty}^{+\infty} \phi(t) dt$ . We have assumed a flat (1D) pulse profile which is valid given the experimental  $2.5 \times 2.5$  mm<sup>2</sup> flat (top hat) beam profile. By time integrating Eq. (9) we arrive at the transient temperature at each point in the multilayer volume. For simplicity, we initially assume a linear (i.e. temperature independent) response, and normalize temperatures to the incident laser fluence  $f$ , i.e. we get the normalized transient in Kcm<sup>2</sup>/mJ (Fig. 4d). By studying the linear heat transport regime we get insight into the temperature transients and gradients that can be developed, without considering nonlinear effects on the materials properties, nor the thermodynamics of phase changes, e.g. melting and resolidification. We also note that regarding radiation and convection losses from the top surface, a simple estimate suffices to show that they are of no consequence. We'll quantify this after we obtain our first estimates on the temperature profiles created during the laser treatment.

For the heat transport calculations we follow the effective medium approach similarly to the optics calculation. We first simulate the explicit multilayer structure formed of 20 repetitions of AlN/Ag bilayers which is described by the individual layer thickness and material parameter. The material parameters  $\rho$ ,  $c$ ,  $k$  are taken from literature [89]. Their values and their optical constants are shown in Table 1. They impose a spatial dependence due to the interchange of different materials. We also simulate the effective multilayer structure described by the total thickness of the multilayer and the effective medium materials parameters. The effective thermal conductivity and capacitance are defined as [90]:

$$k_{eff} = \frac{k_{AIN} k_{Ag} (l_{AIN} + l_{Ag})}{k_{Ag} l_{AIN} + k_{AIN} l_{Ag}} \quad (10)$$

$$(c\rho)_{eff} = f_{AIN} (c_{AIN} \rho_{AIN}) + f_{Ag} (c_{Ag} \rho_{Ag})$$

Thus, we obtain the explicit and effective normalized transient temperatures for the two Ag volume ratios. Comparing explicit and effective transient temperatures we find excellent agreement at each point in the multilayer volume and the substrate for both volume ratios. This agreement is depicted in Fig. 4d in which we compare the transient temperatures at the top of the multilayer. Given the large gain in computational speed, from now on we only use the effective parameters to extract the normalized transient temperatures.

So far we have developed a semi-analytical opto-thermal model which provides the normalized transient temperatures at each point in the multilayer structure. Utilizing this model we calculate the peak temperature spatial distribution from the top of the multilayer down to the Si substrate. Peak temperature can be a critical parameter for the final distribution of the embedded NPs in the dielectric matrix after LA process and is strongly related to the Ag volume ratio, the thermal conductivity of AlN and the total thickness of the multilayer. We continue now by exploring each one of the above parameters.

We plot the absorption spatial distribution (Fig. 5a) and the normalized transient temperatures (Fig. 5b, c and d) of the nano-composite thin film for different thicknesses and dielectric thermal conductivities of AlN.  $k_{AIN}$  is sensitive to the deposition method and conditions and can exhibit a large variation ranging from 2 W/mK for amorphous AlN (a-AlN) [91] to 285 W/mK for high crystalline AlN (w-AlN) [92]. To explore its effect, we plot the temperature transients for several different values of  $k_{AIN}$ . We observe that for low  $k_{AIN}$  values of 2 W/mK (Fig. 5b), increasing the thickness of the nano-composite results into an increase

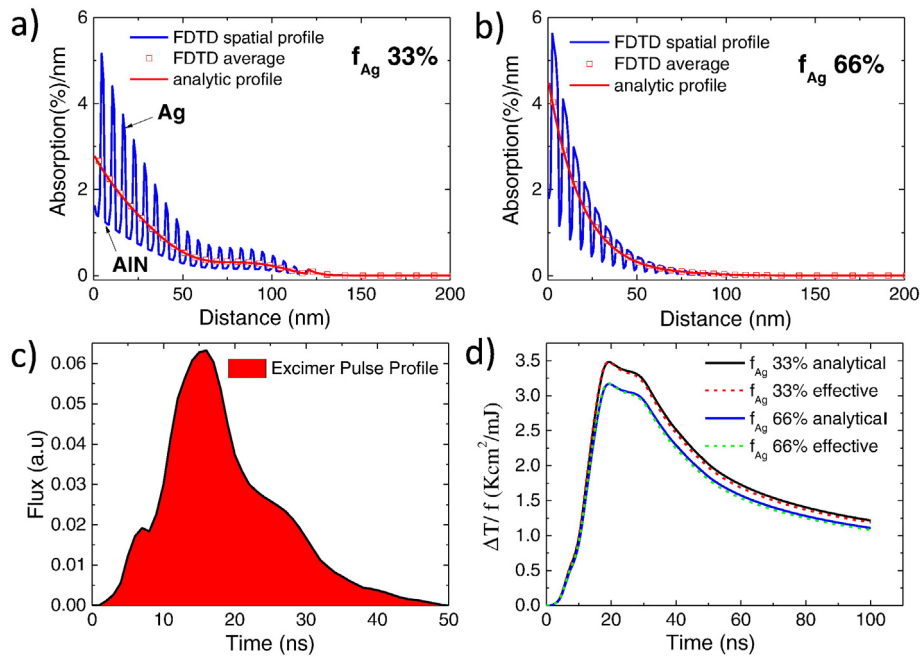


**Fig. 4.** UV (193 nm) absorption spatial distribution in our multilayer structure (20 AlN/Ag bilayers on Si, total thickness 120 nm) extracted numerically (FDTD) and analytically, from the top of the multilayer down to the Si substrate, for two volume ratios of Ag a) 33% and b) 66%. c) The experimental temporal pulse profile of the excimer laser. d) Explicit and effective medium-based normalized temperature transients at the top of the multilayer for the two Ag's volume ratios in a w-AlN matrix (280 W/mK).

of the temperature on the top of the multilayer because of the increase of the total thermal insulation. This effect slows-down for increasing  $k_{AIN}$  and eventually further thickness increments do not significantly affect the temperature (Fig. 5c). Furthermore, for even higher thermal conductivity, e.g. 280 W/mK (Fig. 5d), increasing the nano-composite thickness causes the temperature to decrease because the total effective thermal conductivity is now larger than that of Si, which now becomes the thermal bottleneck. Also in effect is the fact that the thermal capacitance of the composite is larger than that of Si and so increasing its thickness also results into smaller temperatures.

Next, we plot the peak temperature at each point in the multilayer from the top down to the Si substrate (Fig. 6a, b and c) for three  $k_{AIN}$  values. We observe the same trend as we explained before for the normalized transient temperatures. Also, at low  $k_{AIN}$  values (Fig. 6a) we observe that the peak temperature at the first nanometers of the Si substrate decreases for increasing multilayer thickness, because of the slower diffusion of the thermal flux towards the Si substrate (roughly the equivalent of using a wider pulse with the same total pulse energy).

At this point we examine in more detail the effect of  $k_{AIN}$  onto the peak temperature spatial distribution across the multilayer structure and the Si substrate. Here, we assume a wide range of  $k_{AIN}$  (1–400 W/mK) beyond the aforementioned limits (2–285 W/mK) in order to effectively cover with our calculations a wider range of dielectric materials. In doing so, we plot the peak temperature spatial distribution as a function of  $k_{AIN}$  for two multilayer thicknesses, 100 nm (Fig. 7a) and 500 nm (Fig. 7b). We observe that for high  $k_{AIN}$  values the temperature is almost constant across the multilayer. For low  $k_{AIN}$  values on the other hand, a significant temperature gradient is developed across the multilayer, the same trend being observed for both multilayer thicknesses. Higher temperatures close to the surface and lower

temperatures close to the substrate will result into different annealing conditions across the nano-composite thickness. Comparing now the two thicknesses and focusing on the Si substrate we observe that the smaller the thickness is, the higher the temperatures gets at the top of the Si substrate, as we have explained before. We performed the same calculations for a nano-composite of 66% of Ag volume ratio and we observed the same trend, but with lower temperatures due the high thermal conductivity of silver which results into a higher effective thermal conductivity of the multilayer.

The detailed effect of the multilayer thickness onto the peak temperature at the top of the multilayer is shown in Fig. 7c for various values of  $k_{AIN}$ . We observe that for low  $k_{AIN}$  values and small film thickness the temperature increases rapidly with film thickness because of the increased thermal insulation provided by the thicker film, but it saturates for larger films (>200 nm). This effect is less intense for higher  $k_{AIN}$  values, because the effective thermal conductivity is increased. We also observe that for  $k_{AIN} = 80$  W/mK the temperature is almost constant for all the thickness values: here the effective film behaves similarly to silicon, and thus increasing its thickness is of no consequence. Above this value the effect is reversed, i.e. the temperature decreases as the film thickness is increasing. That's because for high  $k_{AIN}$  values the thermal diffusivity is very high and the thermal capacitance becomes the crucial parameter: increasing the thickness, thermal capacitance is increased and thus results to lower temperatures as we mentioned above.

Having estimated the temperatures expected during UV LA, we can now make a simple estimate for the radiation and convection losses from the top surface, and show that they are of no consequence. For example, in the case of  $k_{AIN} = 20$  W/mK and laser fluence of 1000 mJ/cm<sup>2</sup>, a max peak temperature of about 6000 K is achieved (see Fig. 6c). If we

**Table 1**  
Material values used in the opto-thermal calculations.

Material	n	$\kappa$	Mass density ( $\times 10^3$ kg/m <sup>-3</sup> )	Heat capacity (J/kgK)	Thermal conductivity (W/mK)
AlN	1.57	0.19 [79]	3.26	740	10–285
Ag	1.03	1.18 [78]	10.49	235	429
Si	0.88	2.76 [78]	2.33	710	149

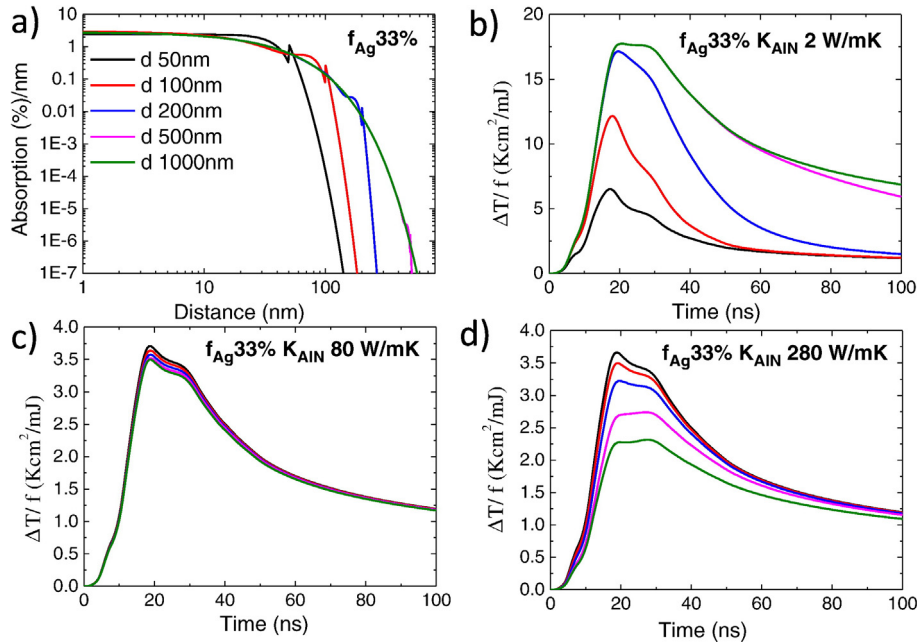


**Fig. 5.** a) UV (193 nm) absorption spatial distribution from the top of the multilayer down to the Si substrate, for five AlN/Ag multilayer thicknesses (50 nm, 100 nm, 200 nm, 500 nm, 1000 nm) extracted from the explicit simulation model. Normalized transient temperatures on the top of the multilayer, for five thicknesses and three AlN thermal conductivities: b) a low value 2 W/mK (a-AlN) c) an average value 80 W/mK and d) a high value 280 W/mK (w-AlN).

further assume the extreme cases of unit thermal emissivity, surface-to-air heat transfer coefficient 200 W/m<sup>2</sup> K (appropriate for forced air cooling [93]) and that this heat exchange with the environment occurs for 30 ns (the approximate pulse duration), we get a total energy loss of about 0.1 mJ/cm<sup>2</sup>, which is 4 orders of magnitude smaller than the input fluence. Thus, radiation and convection at these time scales do not have any effect on the temperature transients and profiles.

One critical oversimplifying assumption up to now has to do with neglecting the fact that the thermal parameters of materials are actually

temperature dependent. The most striking nonlinearity is found in the thermal conductivity of w-AlN, whose change with temperature is shown in Fig. 8a. Other parameters such as thermal capacity and mass density also have a thermal dependence, but of a smaller magnitude. Since the highest temperatures are going to be reached inside the film, and to keep our discussion simple, we ignore the nonlinearities associated with the Si substrate. Utilizing the experimental temperature dependent thermal conductivities of Ag [89] and w-AlN [92] (Fig. 8a) we calculate the non-linear effective thermal conductivity according

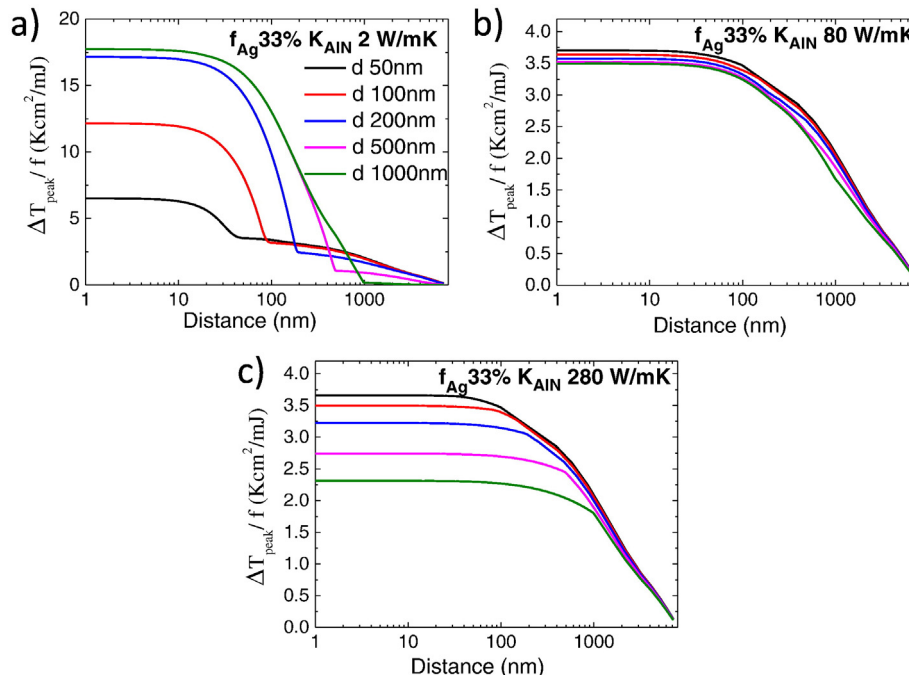


**Fig. 6.** Peak-temperature spatial distribution in the multilayer from the top down to the Si substrate, for three AlN thermal conductivities: a) 2 W/mK b) 80 W/mK and c) 280 W/mK.

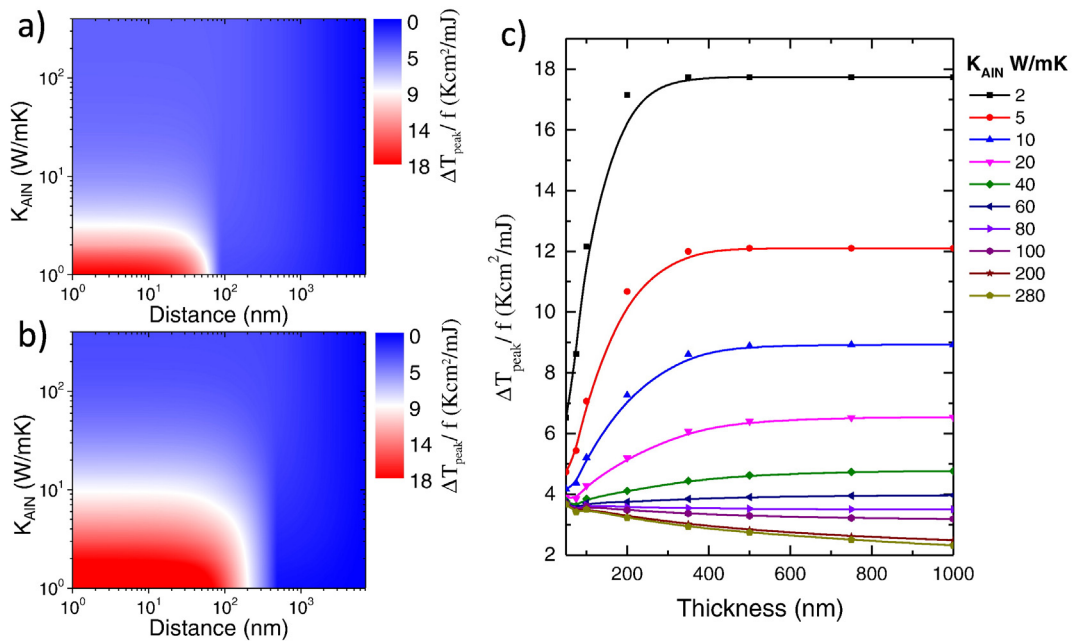


Fig. 7. Map of the peak temperature spatial distribution from the top of the multilayer down to the Si substrate (1 nm – 8 μm) as a function of  $k_{AIN}$  (1–400 W/mK) for two multilayer thicknesses a) 100 nm b) 500 nm. c) The peak temperature on the top of the multilayer as a function of its thickness for various  $k_{AIN}$  values. The silver volume ratio is 33%.

to Eq. (9) for specific Ag volume ratio ( $f_{Ag} = 33\%$ ), depicted by the red points of Fig. 8b. In order to extract the exact effective thermal conductivity at each temperature we fit (black line in Fig. 8b) the experimental temperature dependent effective thermal conductivity with:

$$k_{eff}(T) = k_{eff}(300K) \times aT^b \quad (11)$$

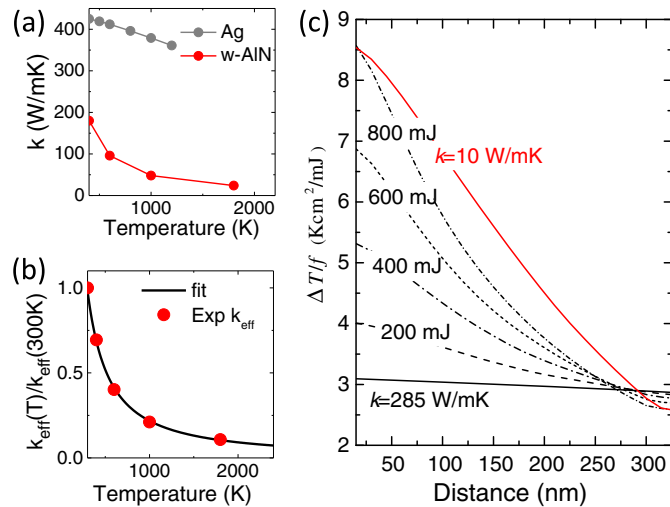


Fig. 8. a) The experimental temperature dependent thermal conductivities of Ag [89] and w-AIN [92] assumed in this work. b) The effective non-linear thermal conductivity obtained from (a) for 33% volume ratio of Ag (red points) on which we perform a fit (black line) to obtain an analytical expression for the non-linear thermal conductivity at each temperature. c) Peak transient temperature distribution as a function of distance from the film's top surface, at different incident laser fluence assuming the nonlinear thermal conductivity for the multilayer structure (w-AIN and Ag from (b)). Broken lines are for nonlinear w-AIN and Ag for different laser fluence. Solid lines are for the linear case (zero fluence limit) for w-AIN ( $k = 285$  W/mK) and for an ultra-low conductance a-AIN ( $k = 10$  W/mK), both for a linear Ag thermal conductivity of 429 W/mK [47]. (For interpretation of the references to colour in this figure legend, the reader is referred to the web version of this article.)

where  $k_{eff}(300K) = 321$  W/mK and  $a, b$  are fitting parameters with  $a = 1233$  and  $b = -1.25$ . Having parametrized the non-linear thermal conductivity we are able to calculate the transient temperatures at each point in the multilayer structure, which we plot in Fig. 8c as a function of distance from the film surface for several different values of laser fluence. For comparison we also plot the linear response of w-AIN (solid black line) and of a linear a-AIN with  $k = 10$  W/mK (solid red line). The nonlinear multilayer lines span the space between the two linear curves as the incident fluence increases. Thus the nonlinearity in thermal conductivity increases the temperature gradients developed in the film. Interestingly, the gradients are generally sharper in the nonlinear w-AIN case (e.g. compare the 800 mJ case with the linear a-AIN  $k = 10$  W/mK case, where the peak surface temperatures are the same), meaning that a composite with a matrix of high thermal conductivity (e.g. w-AIN) will get restructured only close to the film's top surface, while a composite with a matrix of low thermal conductivity (e.g. a-AIN) will get restructured within a wider length inside film. In the next session we will show that this nonlinearity perfectly explains the behavior observed in our recent experiments.

## 2.2. Combined discussion on theory and experiments

In this section we present relevant recent experiments and apply the above-described theoretical opto-thermal modeling. Specifically, we present the results of a single ultra-short UV laser annealing step on a ceramic/metal (in particular AlN/Ag and  $Y_2O_3/Ag$ ) multilayer film. This LA step is capable of driving the subsurface modification of the metallic multilayers resulting into LSPR behavior from NPs that are formed and dispersed in a depth of several nm away from the surface. The multilayers consisting of alternating thin layers of AlN and Ag were fabricated in an in-house built high vacuum system employing the dual cathode reactive magnetron sputtering. The AlN crystal structure was varied in the two sets of AlN/Ag by applying two different power values to the Al target, 100 W and 15 W. This variation leads to different categories of sputtered AlN as indicated from X-ray Diffraction measurements [47]: at 100 W we obtain high crystalline w-AIN while at 15 W we obtain a-AIN. The produced samples were subjected to LA with an excimer ArF source (193 nm, pulse duration of 25 ns). The effect of a single-pulse

LA step onto the structural and optical properties were investigated as a function of fluence ( $400\text{--}700\text{ mJ/cm}^2$ ) in an ambient atmosphere. Fig. 9 illustrates cross sectional Transmission Electron Microscopy (TEM) images showing the morphology of samples before and after LA at  $600\text{ mJ/cm}^2$ .

TEM observations from the as-deposited samples (Fig. 9a and c) verified their multilayer character. In both samples Ag was arranged in 21 layers. After LA treatment the upper part of the multilayer was highly affected. The multilayer structure is destroyed and the enlarged NPs are fairly homogeneously distributed inside the AlN matrix, retaining a high density in the case of a-AlN. On the contrary, in the case of w-AlN only the top of the laser treated part of the sample is affected, and is generally depleted of Ag, indicating a higher diffusivity of Ag in w-AlN compared to a-AlN. In particular, the w-AlN/Ag shows destruction of periodicity affecting only the top six Ag layers, while two more layers are partially destroyed. The sample thickness that retains a stratified arrangement is indicated by a dashed line in the inset of Fig. 9b, which depicts the contrast intensity profile along the film thickness. In the case of a-AlN/Ag, this structural re-arrangement is more extensive as shown in Fig. 9d, and it affects the top ten Ag layers, while again two additional layers are partially affected.

The variation in the NP size distribution and of the total depth of LA process in the films are attributed to the different thermal conductivity  $k_{\text{AlN}}$  of AlN, which is sensitive to the deposition method and conditions, and can show large variations ranging from about  $10\text{ W/mK}$  for amorphous AlN [91] to  $285\text{ W/mK}$  for single crystal [92]. Comparing with our theoretical findings in Fig. 8c, we can confirm that it is the nonlinear character of w-AlN's thermal conductivity that limits the reconstruction only on the top of the multilayer, while the a-AlN case shows extended reconstructions throughout. All the above considerations make AlN's

thermal conductivity a crucial parameter in the LA process and our modeling process a useful tool in its understanding and design.

We conclude this section by modeling and discussing the optical response of the annealed films in connection to the opto-thermal modeling. As expected, the size and distribution of Ag NPs within the amorphous or nanocrystalline AlN matrix determines their LSPR. In Fig. 10a, b we present the experimental optical reflectance spectroscopy (ORS) data from a-AlN and w-AlN, respectively. The optical response of these samples is in agreement with the above mentioned experimental results and the outcomes of the photo-thermal modeling. Indeed, in the case of a-AlN the low  $k_{\text{AlN}}$  values allow for high temperatures to be developed inside the film's volume, and thus to NP enlargement with a broad plasmonic response and a monotonic increase in reflection intensity. At the same time the red-shift of the LSPR spectral position with respect to the fluence can be attributed to either the formation of bigger Ag NPs and/or to the formation of a denser environment, i.e. by changing the refractive index of the host [47]. On the contrary, for the case of w-AlN (Fig. 10b) the narrow reconstruction length, in relation to its nanocrystalline character, leads to a non-monotonic behavior of the LSPR characteristics with respect to the fluence.

To better understand the optical characterization results, we calculated the optical reflectance from a distribution of Ag NPs inside an a-AlN matrix and a w-AlN matrix and compare it with the corresponding experimental ORS of LA processed samples. For computational simplicity we assume the Ag NPs to be arranged in an fcc lattice, for a reconstructed thickness of  $140\text{ nm}$ , leaving five bilayers of  $5\text{ nm Ag}/10\text{ nm w-AlN}$  (i.e.  $75\text{ nm}$ ) unstructured before the Si substrate (see inset in Fig. 11a). We consider three different particle sizes at fixed volume filling ratio of 33%. In Fig. 11a we observe two peaks, the first one is around  $450\text{--}475\text{ nm}$ , it corresponds to NPs' LSPR and for increasing NPs' size it

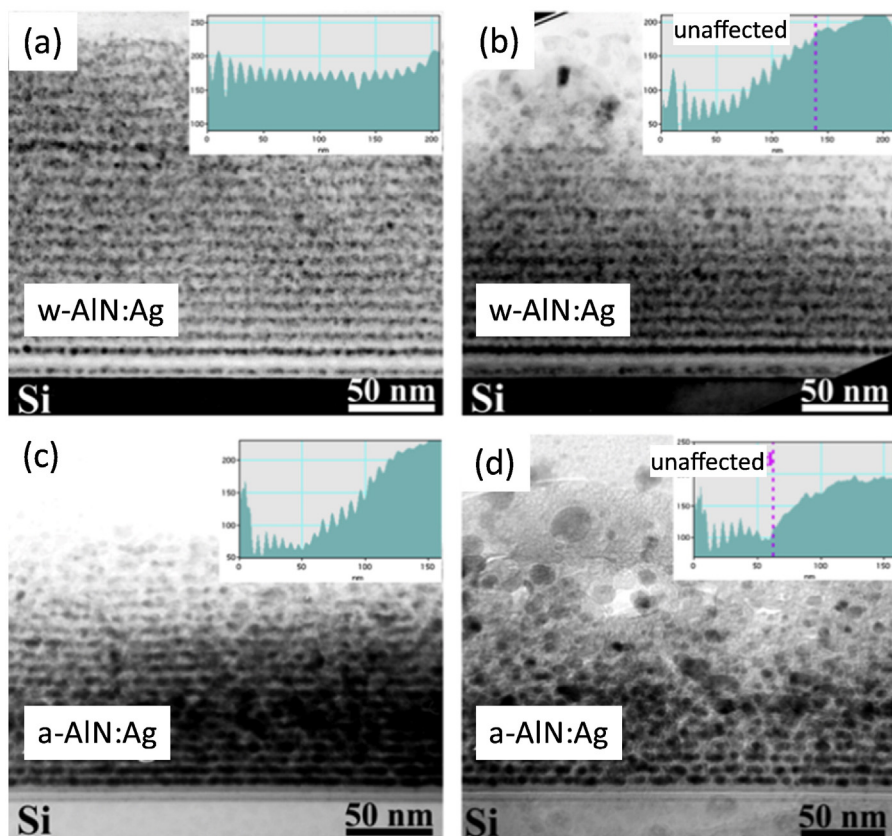


Fig. 9. TEM cross sectional images of: a) the as deposited multilayer structure of w-AlN/Ag, b) the same after LA, and c) the as deposited multilayer structure of a-AlN/Ag, d) the same after LA. LA fluence for all relevant samples in this figure was set to  $600\text{ mJ/cm}^2$  [47].

red-shifts and becomes more intense. The calculated optical response is in good agreement with experimental ORS of the corresponding annealed structure of a-AIN (Fig. 10a) in which we observe that with increasing LA fluence the LSPR slightly red-shifts and becomes more intense. The second peak at 600–625 nm corresponds to multiple reflections in the film. This is verified in Fig. 11c where we observe that after increasing the thickness of the structured NPs arrangement, multiple reflections are differentiated but the LSPR is not, because it depends only on the NP size and distribution. The absence of multiple reflections in the experimental results could be attributed to the high absorbance of the a-AIN matrix which is underestimated in our simulations.

The same trend is observed in the case of the w-AIN matrix (Fig. 11b), in which the NP LSPR is slightly red-shifted and becomes less intense as the NP size increases, in the spectral range of 550–575 nm. This is in good agreement with the corresponding experimental results. The rest of the resonances in Fig. 11b above 700 nm correspond to the film's multiple reflections, as verified in Fig. 11d similarly to the previous case. Multiple reflections are also observed in experimental ORS of w-AIN, which correspond to the dips above 650 nm in Fig. 10b. These are clearer here however because of the lower absorption of high crystalline w-AIN compared with the low crystalline a-AIN. Furthermore, we verify that there is a small red-shift of the LSPR peak as the Ag NP size increases. This is expected: the LSPR of NP arrays red-shifts for increasing NP size and blue-shifts for increasing relative (i.e. distance/radius) NP separation [94]. For a fixed NP volume filling ratio (i.e. assuming no metal is diffused out of the film), however, the relative separation remains fixed, and so we only expect to observe a red-shift with NP size increase.

Finally, we present a demonstration of “plasmonic optical encoding and reading” on a  $Y_2O_3/Ag$  thin film on a Polyethylene Terephthalate (PET) substrate. The  $Y_2O_3$  matrix was chosen because of its low thermal conductivity [95] which works as an efficient barrier protecting the underlying PET film from high temperatures. The digital photo of Fig. 12 represents the sample's appearance in transmission mode under white light illumination (its appearance in reflection mode is also presented in the inset of Fig. 12). Specifically, ‘NTU’ (Nottingham Trent University, who was the academic partner performing the laser annealing experiments) spots were fabricated by delivering 25 pulses of  $15 \text{ mJ/cm}^2$  while the surrounding matrix was fabricated by delivering a single pulse of  $45 \text{ mJ/cm}^2$ . The minimum feature size of this type of ‘plasmonic writing’ is only limited by the LA wavelength and instrumentation, and could thus easily reach the sub-micron regime. This demonstrates the cold character of LA by creating plasmonic templates on flexible polymeric substrates. From the point of view of applications on optical encoding of information, these examples signify the simplicity, flexibility and versatility of the proposed engineering approach. An additional feature of the produced encapsulated plasmonic NP patterns

is their capability of providing two views of the same image with complementary colours in reflection and transmission.

### 3. Surface nano-structuring

#### 3.1. Theoretical approach

Plasmonic templates can be fabricated by LA annealing of a thin metal film on a substrate, resulting into nanoparticle arrangements with many plasmonic applications as we have mentioned in the Introduction. The enabling property of these templates is the coherent surface plasmon oscillations excited by the incident light at specific frequencies, with high selectivity on the metal nanostructure size and shape. But a selective plasmon excitation is necessarily accompanied by selective light absorption, and thus by selective heating of the nanostructure. While this is generally a nuisance for applications, it can be beneficial for the actual template fabrication process: we can use this core property of the target application to become itself one of the drivers in a multi-pulse laser induced self-assembly process, i.e. a repeated heating, melting and resolidification process, driving the NP formation and self-assembly. We keep in mind however that this is not a sole function of light absorption, as different geometries of NP templates will have a different cooling rates. Taking thus into account both the selective heating and the selective cooling as parts of our toolbox, we seek to design and fine-tune the laser-driven self assembly process.

The light absorption mechanisms in the case of nano-structured noble metals such as Ag, Au and Cu, can be generally split into (a) interband absorption from the metal's internal  $d$ -electrons, which is typically enabled at UV frequencies and in general is not size-dependent, and b) resonant intraband absorption, from the conduction electrons due to excitation of LSPR, which is strongly size and shape-selective. As an example, the overall absorption profile of an Ag nanoparticle (hemispherical shape) with diameter of 40 nm on top of a Si substrate is plotted in Fig. 13, showing the spectral domains of the two absorption mechanisms. Utilization of these absorption modes combined with the size selectivity of cooling ( $\sim$  nanostructure surface/volume ratio) constitutes our toolbox for controlling the self-assembly of nanoparticles. Computer simulations will help us explore the potential of these tools by examining NPs of different sizes and arrangements within the UV and optical spectrum. The computational procedure is presented below.

As a starting point, let's assume that after some laser treatment of a thin silver film on a Si substrate, Ag NPs with specific diameters have been formed. Our target is then to consider what will be the effect of a new incoming laser pulse. For computational simplicity we assume a hexagonal lattice of Ag-hemispheres on a Si substrate with different separation aspect ratios  $a/d$  (periodicity/diameter). A schematic of the simulation system is depicted in Fig. 14a. We assume three extreme

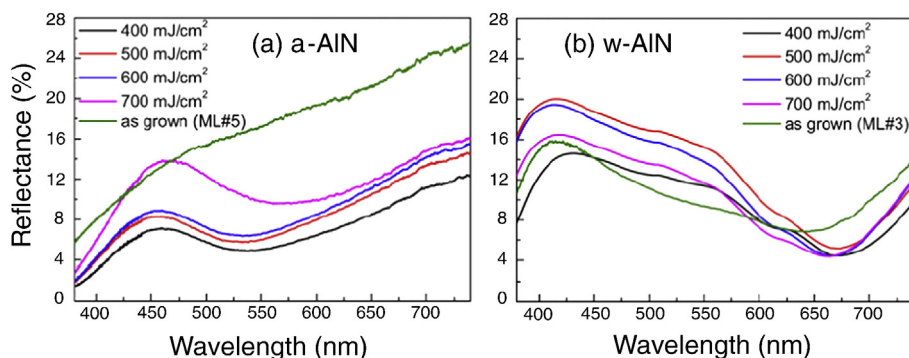
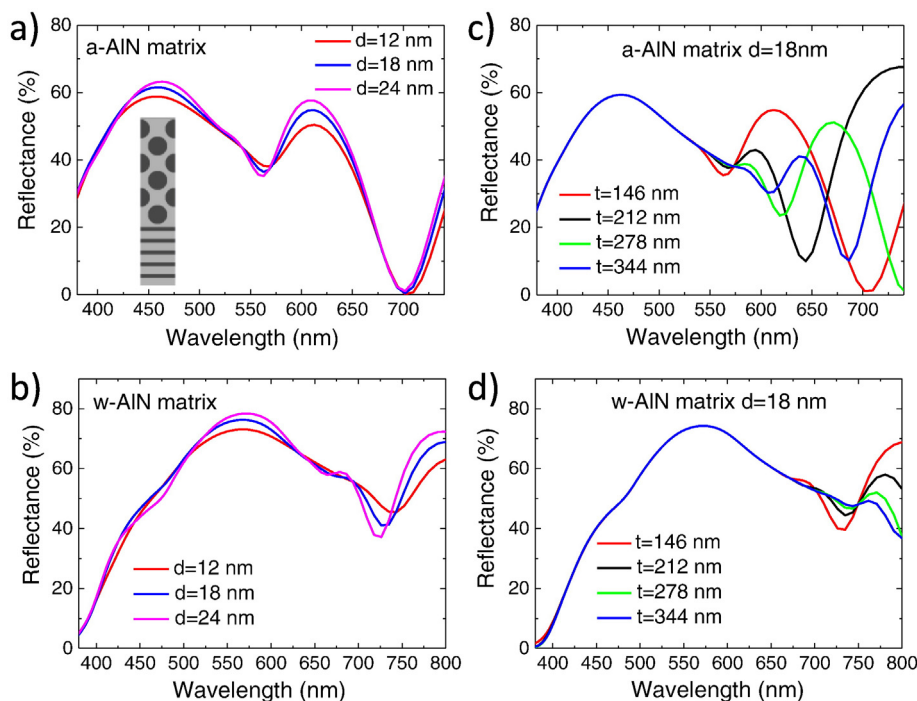


Fig. 10. (a) ORS of LA processed a-AIN/Ag multilayer, (b) ORS of LA processed w-AIN/Ag multilayer. The corresponding spectra from the as-grown samples are also shown for comparison.



**Fig. 11.** Calculated optical response of Ag NPs inside an a) a-AIN and b) w-AIN matrix for three particle sizes. The Ag NPs are arranged in an fcc lattice (Ag volume filling ratio of 33%) extending 140 nm from the surface, leaving five bilayers of 5 nm Ag/10 nm w-AIN (i.e. 75 nm) unstructured before the Si substrate. A projection of the simulated structure for NPs of diameter  $d = 24$  nm is shown in the inset. c) Same configuration as (a) increasing only the thickness  $t$  of the structured Ag NPs arrangement from 146 nm up to 344 nm for the same NPs' size  $d = 18$  nm. d) Same configuration as (b) increasing only the thickness  $t$  of the structured Ag NPs arrangement from 146 nm up to 344 nm for the same NPs' size  $d = 18$  nm.

cases, when NPs are slightly overlapping with each other ( $a/d = 0.9$ ), when the NPs just touch each other ( $a/d = 1$ ), and when the NPs are well isolated ( $a/d = 1.2$ ). A cross section of the final case is illustrated in Fig. 14a. The NP's diameter ranges from 10 nm–120 nm, which span the experimentally relevant sizes as obtained from Atomic Force Microscopy (AFM) and Scanning Electron Microscopy (SEM) images in our recent experiments [65]. We stress here that our theoretical calculations were performed for ordered NPs' arrays at short inter-particle distance below the diffraction limit including the LSPR effects of short-range dipole-dipole interactions, in contrast to ordered and disordered arrays at long inter-particle distance above the diffraction limit which

include the effects of different light diffraction orders on the LSPR features [96].

For the optical calculations, a full-vector 3D FDTD simulator is used in order to capture all possible absorption mechanisms. The absorption spatial distribution is calculated for a wide range of frequencies, in the UV (150 nm–280 nm) and visible spectrum (300 nm–900 nm). The fraction of light absorbed in the sample, expressed as the percentage of the incident radiation absorbed per nm of vertical distance, is calculated (Fig. 14b) for two primary wavelengths:  $\lambda = 248$  nm from an excimer UV laser and  $\lambda = 532$  nm from a Nd:YAG laser. These calculations are for Ag hemispheres of 80 nm diameter. Very efficient UV absorption is obtained for both Ag and Si due to strong direct interband transitions in both materials, while much weaker absorption is found in the visible. We note here that the absorption should in general have a small temperature dependence due to the changing optical constant of Ag (most notably we would expect decreased electron relaxation times at higher temperatures resulting into an increase of UV absorption but a decrease of Vis absorption due to a reduced plasmon line-width),

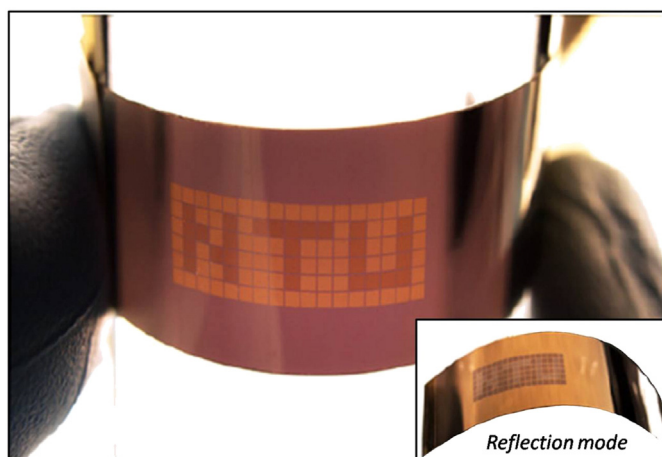


**Fig. 12.** Digital photo of a flexible plasmonic demonstrator capable of optical reading. Photo captured under white light illumination in transmission and reflection (inset) mode. The spots reading 'NTU' were fabricated by LA of the sample with 25 pulses at 15 mJ/cm<sup>2</sup> whereas the surrounding matrix spots were annealed with 1 pulse of 45 mJ/cm<sup>2</sup> [47].

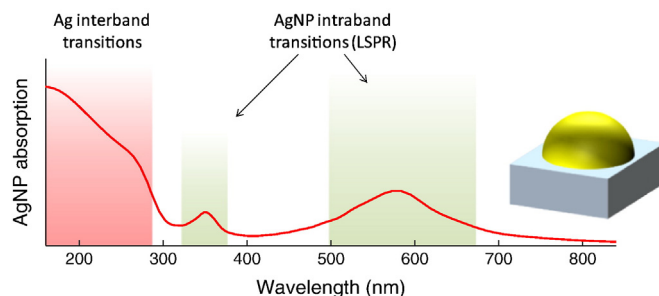


**Fig. 13.** Calculated absorption spectrum of a 40 nm diameter Ag NP on top of a Si substrate, as shown in the inset schematic. Interband absorption dominates the red shaded region, while intraband absorption (LSPR driven) is dominating the green shaded regions (at ~350 nm the quadrupole 428 and ~580 nm the dipole LSPR contributions respectively). (For interpretation of the references to colour in this figure legend, the reader is referred to the web version of this article.)

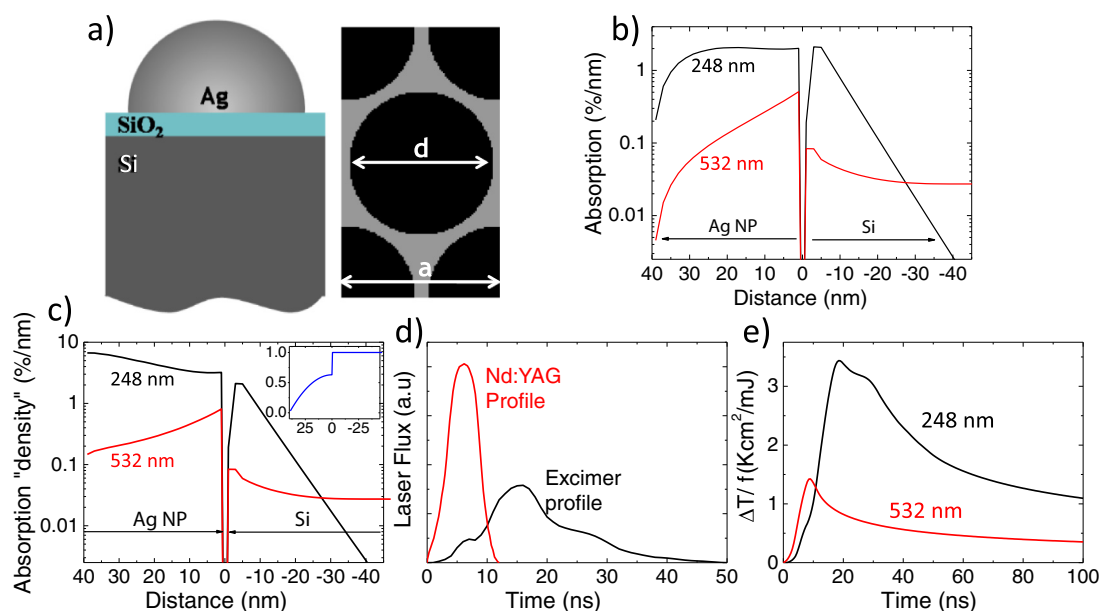


**Fig. 14.** a) Schematic of the simulation system, front view and top view respectively, involving a hexagonal lattice of Ag hemispherical NPs at a period  $a$  to diameter  $d$  ratio 1.2. b) Absorption percentage per nm from the top of the NP (diameter 80 nm) down to the Si substrate, for the two main LA wavelengths. c) Absorption "density" (%/nm) which is produced from the absorption spatial distribution in (b) normalized by the absorbing cross sectional area of the NP (inset graph). d) The laser pulse temporal profiles assumed in the theoretical study correspond to that of an excimer laser (for the 150–280 nm range) or that of a Nd:YAG (for the 300–900 nm range). Both profiles were experimentally determined. e) Normalized transient temperature rise (in degrees per mJ laser fluence) at the NP center for the 80 nm Ag dome for the two LA wavelengths.

but for simplicity we will restrict ourselves to the linear case. For demonstration reasons, this absorption spatial distribution can be normalized by the corresponding cross-sectional absorbing area of the NP (inset graph of Fig. 14c), to get the phenomenological absorption "density" (Fig. 14c).

The absorption spatial distribution is then time-integrated with the appropriate laser temporal profile for each wavelength, depicted in Fig. 14d (excimer for the 150–180 nm range and Nd:YAG for the 300–900 nm range), in a numerical solution of the 1D heat diffusion equation presented in Eq. (9). Thus, we get the temperature transient profile at every point in the structure in degrees/mJ laser fluence. In Fig. 14e we plot the temperature transients for the two primary wavelengths used in our recent experimental study. This way we map the maximum temperature rise as a function of particle size, laser wavelength and laser fluence. As a higher temperature for a particular size group means the melting of this group and the survival of the others, these maps can provide a recipe that allows the design of the annealing process.

First, we explore the different absorption mechanisms which are size selective and enable geometric specificity. In Fig. 15a we present the absorption spatial distribution as a function of wavelength from the top of the NP down to the Si substrate for three NP's diameters. At the UV zone (150 nm–280 nm) the absorption is taking place through the interband transitions of Ag's  $d$ -electrons. We observe that by increasing the NP size, most of the absorption is taking place inside the NP volume and less in the Si substrate. On the other hand, in the optical zone (300 nm–900 nm) most of the absorption is taking place through the LSPR intraband transitions of the metal's free electrons and we observe different resonances. To identify these resonances we plot (Fig. 15b) a vertical cross section of the  $E$  field distribution taken in the middle of the NP, a horizontal cross section of the  $E$  field distribution taken at specific points on the NP volume, as well as vertical cross sections of the logarithmic  $E$  field enhancement  $\log_{10}(|E(x)|^2/|E_0(x)|^2)$ . In Fig. 15b.i we observe a dipole resonance which is mostly localized at the bottom of the NP and related to the NP free electron oscillations dielectrically screened by the substrate. We also notice in the absorption profiles the well known red shift as the NP diameter is increased, accompanied by a reduction in absorption. The other resonances between 345 nm–400 nm (Fig. 15b.ii, iii) are located within the NP's volume and involve

higher order LSPR modes screened mostly by the substrate (ii) or a dipole LSPR in the upper part of the NP screened mostly by the surrounding air (iii). Also, for big NPs we observe a new clear quadrupole resonance (iv) which is located on the bottom of the NP and is related to the NP's free electron oscillations near the substrate (Fig. 15b.iv).

There is an interesting non-obvious detail regarding the intraband resonances which is revealed in Fig. 16: at the exact resonance wavelength we get a lower overall temperature. This is due to the fact that there the reflection is significantly enhanced and thus the overall absorption ( $1 - \text{reflection}$ ) is significantly reduced. However, at slightly longer wavelengths the overall reflection is reduced (the absorption in metal NPs at resonance wavelengths is red-shifted compared to the reflection, with the red-shift increasing for large NPs) and the temperature reaches a peak. The absorption in Si substrate is also enhanced due the near-field enhancement in the vicinity of the Ag NPs, at the resonance wavelength. The combination of the two different material absorptions results into the wavelength dependence of the peak temperature. This feature provides an interesting mechanism for size control, whereby the NPs whose LSPR falls exactly at the same wavelength of the LA, will have enhanced reflection and less absorption, resulting into lower temperatures rises.

Understanding the maximum temperature rise as a function of particle size and wavelength is thus of critical importance. Towards this goal, we plot the optical response (Fig. 17) as a function of NPs' diameter (10–120 nm) and wavelength for two NPs' arrangements. The first one is when the NPs are slightly overlapping or just touching each other (Fig. 17a) and the second one when the NPs are fairly isolated (Fig. 17b). In the first spectral range (300–450 nm) we observe high reflectance especially for the small NPs of the first case (Fig. 17a) where the metallic NPs pose an almost uniform metallic surface. Increasing the size we observe the aforementioned resonances which involve a higher order LSPR modes screened mostly by the substrate (Fig. 16.ii) or a dipole LSPR localized in the upper part of the NP screened mostly by the surrounding air (Fig. 16.iii), which is depicted in the NPs absorption. Also in this spectral range Si is characterized by high absorption which is depicted in both cases (Fig. 17a, b). Also notice that the absorption in Si decreases in the spectral ranges of maximum reflection, as was mentioned before.

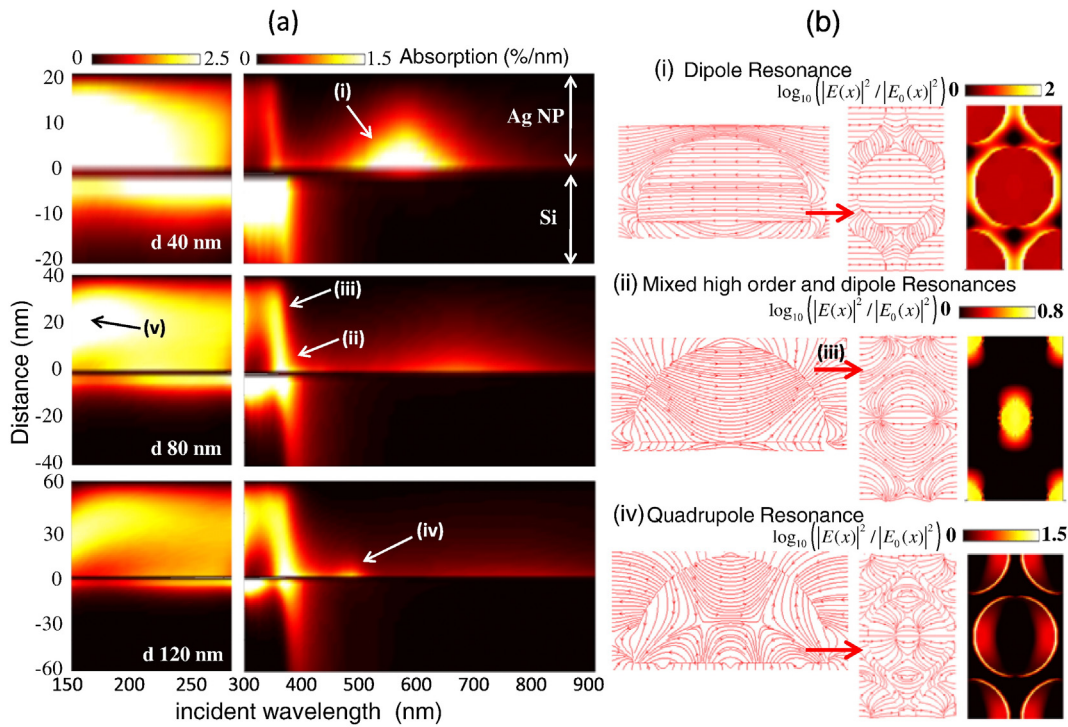


**Fig. 15.** a) Colour map of the absorption profile (in percent per nm) from the top of the NP down to the Si substrate for three NP diameters (40 nm, 80 nm, 120 nm) at separation aspect ratio  $a/d = 1.2$ , plotted for UV (150 nm–280 nm) and UV–NIR (300 nm–900 nm) wavelengths. The inset arrows show the main absorption mechanisms, the first four (i, ii, iii, iv) are related to Ag intraband transitions and the fifth (v) is related to Ag interband transition. b) Electric field spatial distribution plotted at vertical (in the middle of NP) and horizontal (in specified positions on NP’s volume shown by the red arrows) cross sectional planes, at resonance wavelengths, in order to identify the intraband resonances. The colour maps are the horizontal cross sections of electric field’s enhancement. Both of them are shown for the corresponding size depicted by the arrows in (a). The resonances are: (i) dipole LSPR located at the bottom of the NP (573 nm), (ii, iii) mixed high order (365 nm) and dipole (345 nm) resonances located throughout the NP’s volume, (iv) quadrupole resonance (484 nm) located at the bottom of the NP, but clearly seen only for big NPs’. (For interpretation of the references to colour in this figure legend, the reader is referred to the web version of this article.)

In the second spectral range (450 nm–900 nm) we observe that the reflection increases and red-shifts as the NP size increases, due to the dipole LSPR mode (Fig. 16.i).

Taking into account the absorption spatial profile from the top of the NP down to the Si substrate, for each NP between 10 nm–120 nm and

for both arrangements, we arrive at the map of the maximum temperature rise as a function of NP size and wavelength, utilizing in each spectrum the appropriate laser temporal profile (Fig. 18). In these maps we can distinguish areas of higher and lower temperature. We can use this map as a guide to sequentially tune the LA wavelength to match with

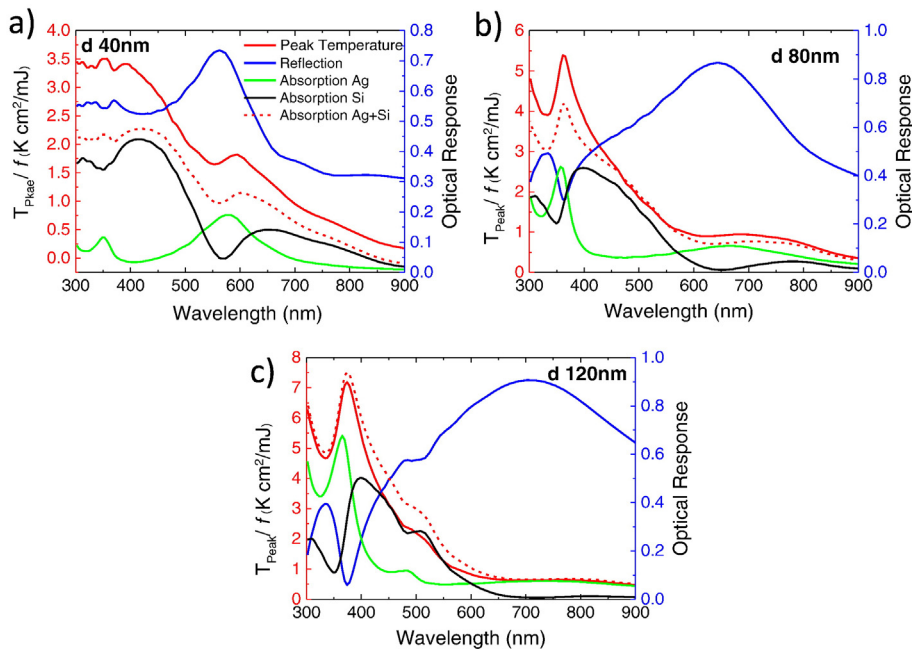


**Fig. 16.** The peak temperature at the middle of the NP as a function of wavelength, plotted in the red axes and the reflection/absorption taking place in Ag NPs, absorption taking place in the Si substrate and the sum of the two absorptions, plotted in blue axes. The separation aspect ratio of the hemispheres is  $a/d = 1.2$  for NP arrangements of a) 40 nm b) 80 nm and c) 120 nm diameter. (For interpretation of the references to colour in this figure legend, the reader is referred to the web version of this article.)

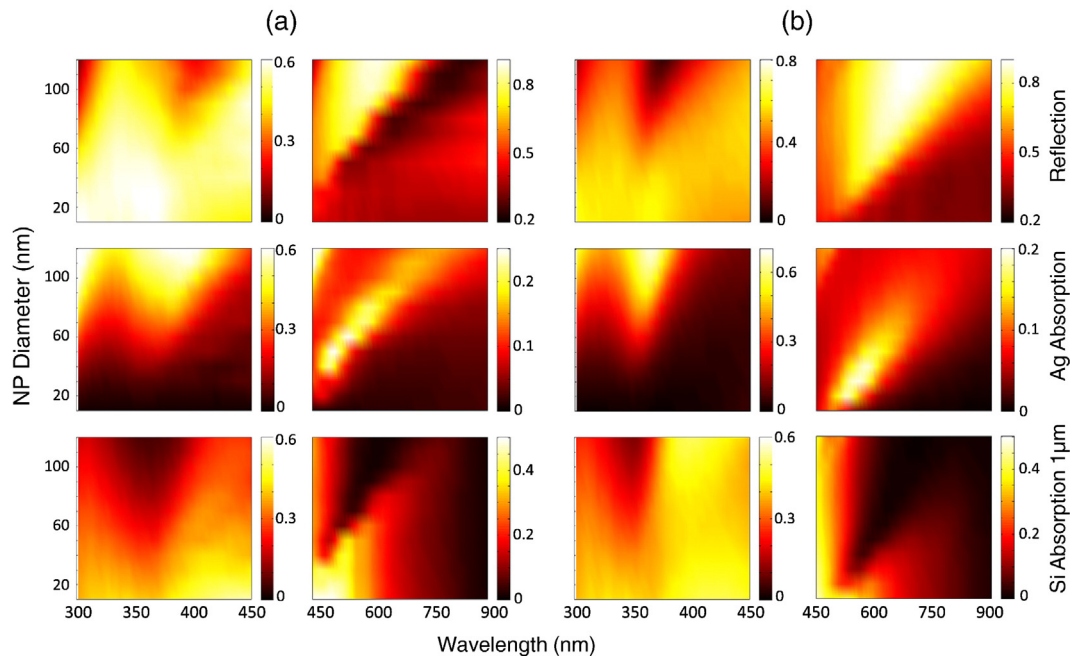


**Fig. 17.** The size dependent optical response as a function of wavelength in the near UV zone (300 nm–450 nm) and visible zone (450 nm–900 nm): a) an average of NPs slightly overlapping each other ( $a/d = 0.9$ ) and of NPs touching each other ( $a/d = 1$ ), b) NPs fairly isolated ( $a/d = 1.2$ ).

different absorption mechanisms and determine the proper laser power that should be applied in order to selectively target the selective heating of different particle size groups. Specifically, in the UV zone utilizing the interband transitions we can remove the larger NPs and arrive at nanostructures with smaller size distributions. In near-UV, utilizing the

intraband LSPR transitions, especially the higher order resonances, we can also remove the large NPs. Finally, small NPs can be removed in the visible zone utilizing dipole LSPR resonance.

Tailoring of ellipsoidal Au and Ag NPs on insulating dielectric substrates with a ns-pulsed laser light (Nd:YAG) has also been reported

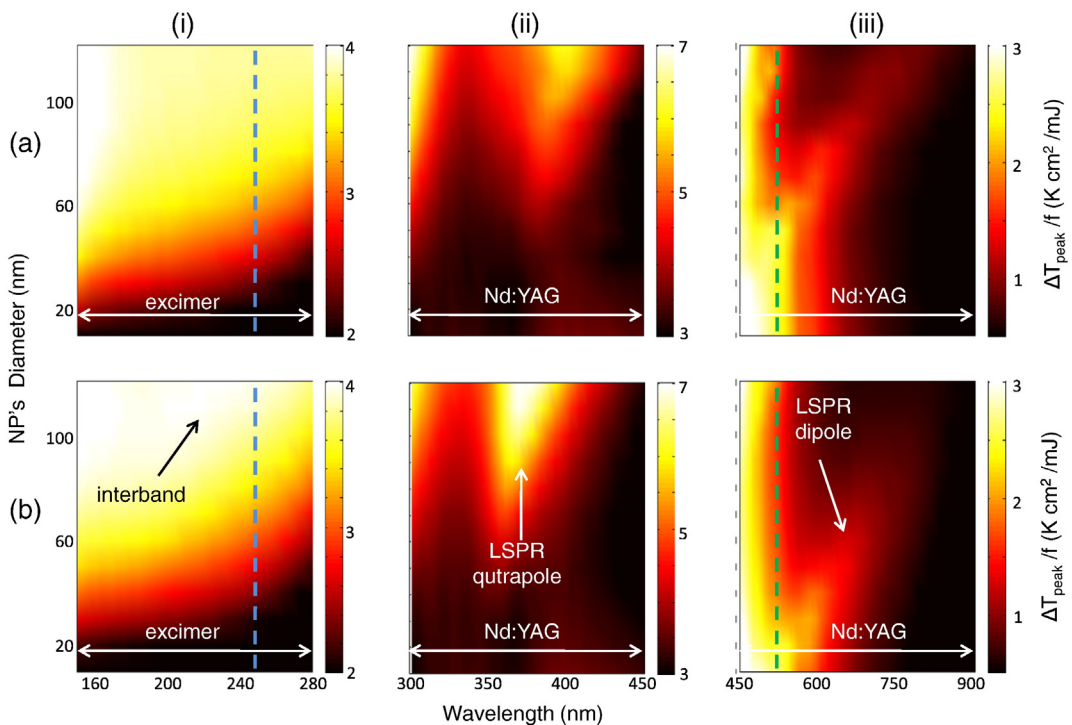


**Fig. 18.** Normalized peak temperature as a function of irradiation wavelength and NP's size for two arrangements: a) an average of NPs slightly overlapping each other ( $a/d = 0.9$ ) and of NPs attaching each other ( $a/d = 1$ ), b) NPs fairly isolated ( $a/d = 1.2$ ). These are plotted in the three wavelength zones: i) UV zone (150 nm–280 nm) utilizing the excimer temporal profile, ii) near UV zone (300 nm - 450 nm) utilizing the Nd:YAG temporal profile and iii) visible zone (450 nm - 900 nm) utilizing the Nd:YAG temporal profile. Indicated with the two dashed lines are the two primary laser wavelengths used in this study, i.e. the 248 nm excimer laser and 532 nm Nd:YAG laser. The different heating regimes are attributed to the different absorption modes and different cooling geometries and can be utilized to tailor-design the LA process.

in literature [97] by utilizing the NP size- and shape- depended intraband absorption. In that work the LA is done in two steps: in the first step the template is laser-irradiated at the large NPs' transverse LSPR wavelength position leading to the stimulated evaporation of NPs' surface atoms. Thus, the size of the specific NPs decreases and their shape becomes more spherical, shifting the spectral position of LSPR and thus self-limiting the laser structuring. In the second step the ensemble is laser-irradiated at the small NPs' LSPR wavelength and for a sufficient high fluence the temperature increase leads to a complete evaporation of these particles. The above procedure results into a substantial amount of metal loss (>40%) with a corresponding reduction in the extinction amplitude from an initial 37% to a final 23%. Here, we follow a modified approach exploring two different absorption mechanisms (interband and intraband) and the fast heat dissipation of the laser induced energy into the Si substrate (as shown in the transient temperatures of Fig. 14e) which significantly limits the ablation of the metal.

To conclude, by appropriately combining different selective heating pathways we can target the melting and re-crystallization of specific NP size groups and arrive at nanostructures with predesigned morphology.

This is the main concept behind our approach: repeated laser treatments, targeting different nanoparticle size groups with different laser wavelengths, driving the size distribution to a final predetermined one. We call this process MONA-LISA: Modification of Nanoparticle Arrays by Laser Induced Self Assembly.

### 3.2. Combined discussion on theory and experiments

We now present the recent experimental demonstration of MONA-LISA. The first step is a single shot UV LA to initialize nanoparticle formation from a semi-continuous metal thin film, by Laser Induced Self-Assembly (LISA). This results into the restructuring of the silver thin film into nanoparticle arrangements in macroscopic scales (several mm<sup>2</sup>). The LISA process with a UV laser (248 nm) is strongly fluence-dependent as demonstrated in the SEM images of Fig. 19a. The Ag NP size distributions are generally bimodal, consisting of one set of coarse and one set of fine NPs. Increasing the laser fluence from 350 mJ/cm<sup>2</sup> to 800 mJ/cm<sup>2</sup> results into a decreasing difference between the two NP sets, as shown by the quantified SEM images (Fig. 19c, purple, cyan, yellow and red lines). The modification of NP assemblies by multiple laser

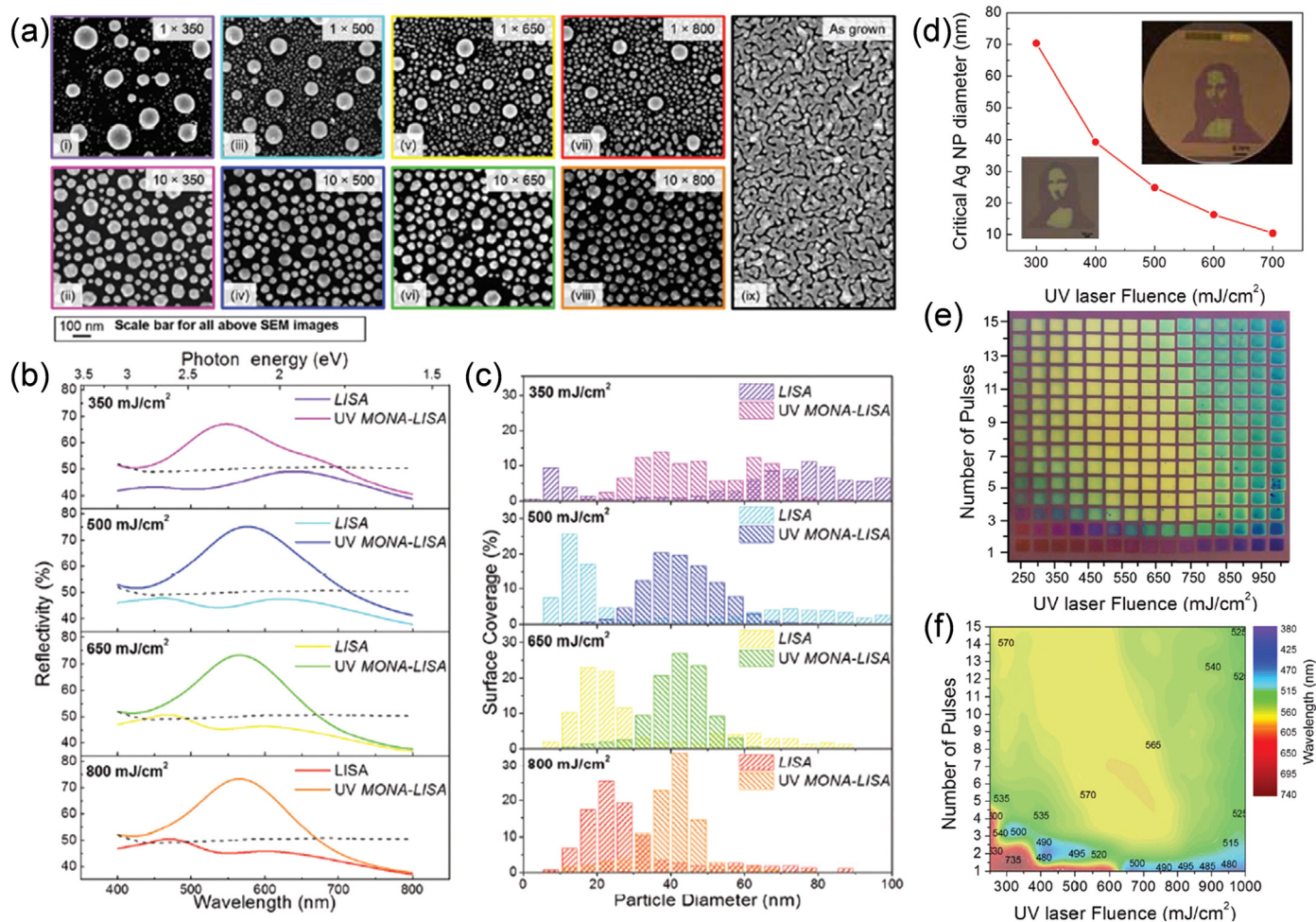


**Fig. 19.** a) SEM images of samples processed with LISA (1 pulse, 248 nm LA) and UV MONA-LISA (10 pulses, 248 nm) under various applied fluences. b) The effect of LISA and UV MONA-LISA on the optical reflectivity spectra of a 10 nm Ag thin film under various applied fluences. c) NP surface coverage as a function of particle diameter for all cases of (a). d) Critical NP diameter (the diameter value under which a NP remains practically cold during the UV LA process, indicating those that cannot be further manipulated upon irradiation) as a function of applied laser fluence. Inset depicts two portraits of Da Vinci's Mona Lisa: Upper inset is a macroscopic, large-scale pattern engraved on a full 2" Si wafer coated with 10 nm Ag (purple areas correspond to a process of one pulse at 500 mJ/cm<sup>2</sup> whereas the green areas to three pulses of the same fluence). Lower inset is a microscopic pattern engraved on the same wafer in a single pixel processing using series of photolithographic masks. e) A digital photo of a grid of LISA/UV MONA-LISA spots of varying fluence (x-axis) and number of pulses (y-axis) produced on a 10 nm Ag thin film. f) Contour plot of the dominant LSPR peak obtained by optical reflectivity spectra from each spot of (e) (in the case of bimodal responses the maximum reflectivity response is reported) [65]. (For interpretation of the references to colour in this figure legend, the reader is referred to the web version of this article.)

pulses involves the utilization of the selective optical absorption and the heat dissipation, as presented in the theoretical approach above. In order to demonstrate this, we subject the initial assemblies of NPs to a series of UV and/or Vis LA steps.

First, we consider the case of UV MONA-LISA, i.e. processing by multiple UV (248 nm) laser pulses, and we correlate the effect of interband absorption with the size-selective heat dissipation. Fig. 19b shows the optical reflectivity spectra of a 10 nm Ag film recorded after UV MONA-LISA using 10 successive UV laser pulses at various fluences (magenta, blue, green and orange lines for 350, 500, 650, 800 mJ/cm<sup>2</sup> respectively). Comparing these spectra with those from the previous LISA processing, reveals that the consecutive pulses transform the two reflectivity peaks into one, indicating a gradual transformation of the bimodal distributions into unimodal ones. This is also confirmed by the corresponding SEM images and the size distribution histograms in Fig. 19a and c (magenta, blue, green and orange bars), respectively. The reshaping of the particles is predominantly due to the disappearance of the larger particles. The physics behind that observation is based on the stronger heating of the larger NPs and faster heat dissipation from the finer NPs due to their higher effective surface (surface to volume ratio). As a result, the finer nanoparticles remain cold during UV MONA-LISA. This was quantified correctly by our photothermal calculations, which yielded the equi-temperature contour lines vs nanoparticle diameter that determine the critical size under which every particle remains practically cold during the UV MONA-LISA process of Ag on Si. Assuming for simplicity the bulk Ag melting temperature of 960 °C, the calculated values of the critical diameter vs fluence for the 248 nm laser are presented in Fig. 19d. Note that the critical diameter strongly depends on the thermal conductivity of the substrate, as a less conductive substrate would hinder heat dissipation. The UV MONA-LISA process is thus based on the larger particles having the ability to raise their temperature above their melting point, and consequently melting and re-solidifying forming smaller particles with a stochastic size distribution, while the smaller ones remain below the melting threshold and therefore remain practically unaffected. Eventually, successive pulses suppress the population of the coarse particles, gradually transforming them to stable fine particles via stochastic size redistribution. The wide range of size distributions achieved by LISA and UV MONA-LISA results into a vast colour palette of plasmonic responses as those presented in Fig. 2e and f (real colour appearance of the Ag nanoparticle assemblies and quantitative spectral reflectivity response, respectively). Combining the LISA and MONA-LISA process with projection masks, enabled the production of multicolour images of high spatial resolution and colour contrast as the one presented in the inset of Fig. 19d, depicting two portraits of Da-Vinci's "Mona Lisa".

The implementation of MONA-LISA employing exclusively UV pulses has the inherent limitation of the UV absorption being rather insensitive to nanoparticle size, and as a result the size selectivity of the process is based exclusively on the size selectivity of the heat dissipation. This has the consequence that only the coarse particles are affected after successive laser pulses. In order to probe and manipulate the finer particles we must exploit their selective optical absorption via LSPR using a visible laser wavelength that would result in stronger optical absorption and hence higher temperature rise, as predicted by the computational results presented in the previous section in Fig. 18. The optimum condition of narrowing the bandwidth of the LSPR at 532 nm was achieved by applying 500 pulses at 125 mJ/cm<sup>2</sup> which shows that the VIS MONA-LISA is slower compared to the UV MONA-LISA that reached at steady state at 10 pulses. This is well expected considering the computational results of Fig. 18, where a lower temperature rise is evident at visible wavelengths compare to UV processing.

Exploring the VIS-MONALISA we start from a UV LISA process (248 nm, 2 pulses at 350 mJ/cm<sup>2</sup>) which demonstrates a double reflectance peak due to its bimodal nanostructuring, notably with no

particular response close to 532 nm, as shown in Fig. 20a (black line). Applying, VIS MONA-LISA to this area, with 500 pulses (i), 2000 pulses (ii) and 4000 pulses (iii) results in gradually changing the bimodal distribution to one with a peak very close to the laser processing wavelength (532 nm). The corresponding SEM images are shown in Fig. 20c, d, e, f. Analysis of these SEM images results into the histograms of Fig. 20b. It is noteworthy that the VIS MONA-LISA probes primarily the finer Ag nanoparticles (<20 nm) confirming the computational analysis presented in Fig. 18.b. As seen in the SEM images, our theoretical assumption of NPs in a fairly isolated arrangement at separation aspect ratio ( $a/d = 1.2$ ) is in close agreement with the experimental case.

## 4. Conclusions

### 4.1. Sub-surface nano-structuring

Functional plasmonic templates consisting of embedded NPs in a dielectric matrix can be fabricated by LA of a stratified metal/dielectric nano-composite. We performed an extensive theoretical investigation to highlight the underline physics of laser induced sub-surface plasmonic nano-structuring. First, we developed an accurate semi-analytical model to estimate the photo-thermal processes involved. Using this model, we calculated the transient temperature distribution at each point in the multilayer structure. We found that it strongly depends on the structure parameters like the metal volume ratio, the total thickness of the multilayer film and the thermal conductivity of the dielectric. By properly designing these parameters, combined with tuning the LA conditions (wavelength and fluence) one can arrive at plasmonic templates with predetermined morphology and optical response. The latter was demonstrated in the experiments in which multilayers of alternating AlN/Ag layers were subjected UV LA (193 nm), leading to a subsurface formation of plasmonic NPs inside AlN matrix with a localized surface plasmon resonance response. The effect of LA on the structural modification and the resulting optical properties of the films was investigated as a function of laser fluence under ambient atmosphere. We found that a parameter that majorly affects the annealing process and determines the resulting reconstruction is the thermal conductivity of the dielectric medium, which provides an interesting route for tailoring the optical response of such structures.

The aforementioned photo-thermal modeling was performed to investigate the laser-matter interactions and heat diffusion in the metal/ceramic multilayers upon LA. The theoretical results covered an extensive range of values in order to present a generic study for different dielectrics. They revealed the paramount role of the thermal conductivity of the dielectric as well as of the relative content of the metal/dielectric components within the multilayer. In particular, low values ( $\alpha$ -AlN and Y<sub>2</sub>O<sub>3</sub>) lead to a significant temperature gradient across the multilayer structure resulting into broadband size distributions for the Ag particles. On the contrary, high  $k$  values (such as in the case of w-AlN) lead to a narrower size distribution of Ag particles within a shallower depth from the film surface. The developed temperature gradient is strongly affected by nonlinearities in material properties, and is also affected by the individual layer thickness and in particular the thickness ratio between Ag and the dielectric in one bilayer: due to the high thermal conductivity of Ag, the higher the Ag content is, the smaller the temperature gradients are within the film, even for low values of the dielectric thermal conductivity.

Furthermore, the optical response of the produced plasmonic nano-composites can be tuned by the fluence of LA as it is shown from experimental ORS and confirmed from FDTD calculations. Specifically, increasing the fluence in the LA process, larger NPs are produced with higher reflectance values and red-shifted LSPRs. Finally, we demonstrated the cold character of LA by creating plasmonic templates on flexible polymeric substrates. From the point of view of applications on optical encoding of information, these examples signify the simplicity,

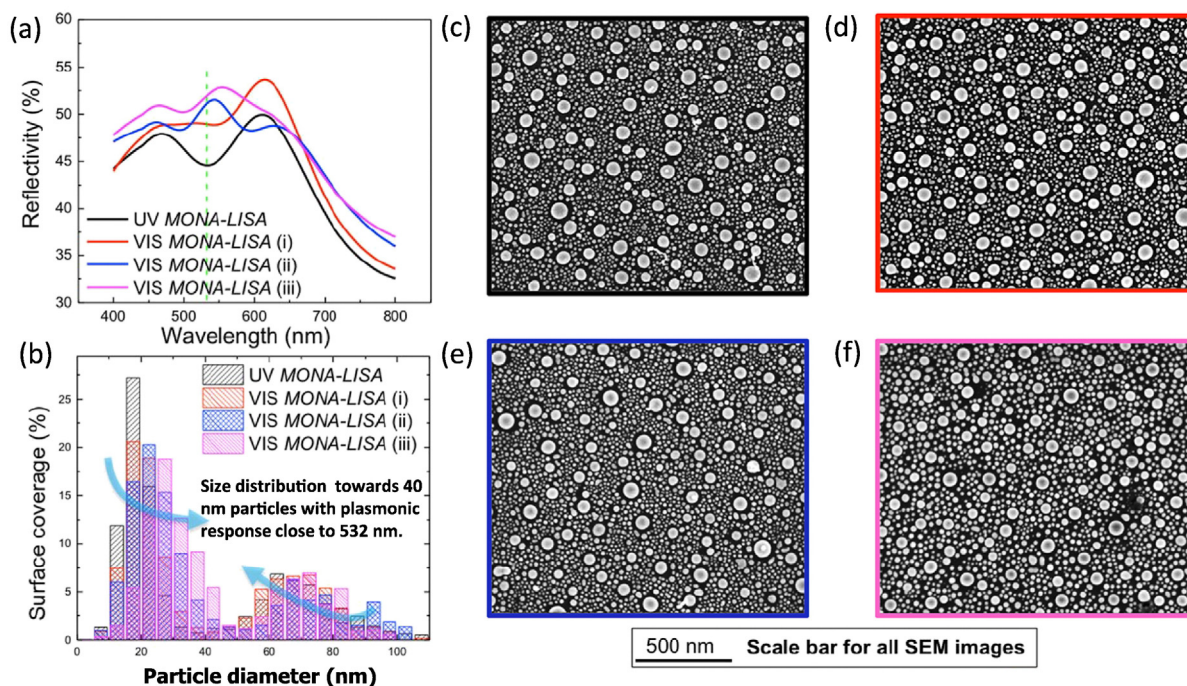


**Fig. 20.** a) Optical reflectivity spectra of LISA (2 pulse, 248 nm at 350 mJ/cm<sup>2</sup> - black line), used as a template for the subsequent Visible MONA-LISA (500 pulses (red line), 2000 pulses (blue line) and 4000 pulses (magenta line), 532 nm at 125 mJ/cm<sup>2</sup>). The green dashed line sets the 532 nm mark. b) Surface coverage of the nanoparticles in relation to the particle diameter for each laser treatment of (a). c) SEM image of LISA processed sample. d) SEM image of the Visible MONA-LISA (i) sample (500 pulses). e) SEM image of the Visible MONA-LISA (ii) sample (2000 pulses) and f) SEM image of the Visible MONA-LISA (iii) sample (4000 pulses) [65]. (For interpretation of the references to colour in this figure legend, the reader is referred to the web version of this article.)

flexibility and versatility of the proposed engineering approach. An additional feature of the produced encapsulated plasmonic NP patterns is their capability of providing two views of the same image with complementary colours in reflection and transmission.

#### 4.2. Surface nano-structuring

Functional plasmonic templates consisting of metallic NPs on a substrate can be fabricated by LA of a thin metal film on the substrate. We performed an extensive theoretical investigation to highlight the photo-thermal processes involved in laser induced surface plasmonic nano-structuring. Specifically, we explored templates consisting of hemi-spherical Ag NPs on Si substrate for different NPs arrangements and sizes, for both UV and optical irradiation. We found and identified different absorption mechanisms which are size selective and enable geometric specificity such as: a) interband absorption taking place at the UV zone, probing the metal's internal *d*-electrons and b) intraband absorption taking place at the near-UV and visible zone, probing the metal's free electrons at the LSPR frequencies.

Then, we performed heat diffusion simulations combining the absorption spatial profile found from the optical calculations with the appropriate experimental laser temporal profile and obtained a map of the maximum temperature rise as a function of particle size, laser wavelength and laser fluence. In these maps we distinguish spectral regions of higher and lower temperature which can be used to provide a recipe that allows designing the modification of NP configuration towards a pre-designed one. In particular, by sequentially tuning the laser wavelength into resonance with different physical absorptions we can selectively target the melting and re-solidification of different particle size groups. This idea was implemented in experiments, in which repeated laser treatments targeted different NPs size groups with different laser wavelengths and drove the final size distribution. Specifically, in the experiments, successive pulses of UV LA reduced the volume fraction of larger nanoparticles (> 50 nm) while VIS LA further refined the size distributions by reducing the volume fraction of the smaller nanoparticles

(<20 nm). This combined UV and VIS LA treatment provides control on the size distributions and plasmonic behavior of nanoparticle arrays of noble metals.

#### Acknowledgements

D.V. Bellas and A. Siozios acknowledge funding from the following sources: the European Union (European Social Fund – ESF) and Greek National Funds through the Operational Program “Education and Lifelong Learning” of the National Strategic Reference Framework (NSRF) - Research Funding Program: Heracleitus II.

The research activities of E. Lidorikis and P. Patsalas that led to these results were co-financed by Hellenic Funds and by the European Regional Development Fund (ERDF) under the Hellenic National Strategic Reference Framework (NSRF) 2007-2013, according to contract no. 11ΣΥΝ-5-1280 of the Project ‘Nano-Hybrid’, within the Program ‘Competitiveness and Entrepreneurship’.

N. Kalfagiannis acknowledges funding from People Programme (Marie Curie Actions) LASER-PLASMON of the European Union's Seventh Framework Programme (FP7/2007-2013) under REA grant agreement no. PIEF-GA-2012-330444.

D.C. Koutsogeorgis acknowledges the School of Science and Technology at Nottingham Trent University for the approval of a sabbatical made possible via QR funds, and the Higher Education Funding Council for England (HEFCE) for providing the QR funds as a result of the Research Assessment Exercise 2008 (RAE2008).

P. Nikolaou and P.C. Kelires acknowledge support by the Strategic Infrastructure Project NEW INFRASTRUCTURE/ΣΤΡΑΤΗΓΙΚΟ/0308/04 of DESMI 2008, which is co-financed by the European Regional Development Fund, the European Social Fund, the Cohesion Fund and the Research Promotion Foundation of the Republic of Cyprus.

The authors would like to acknowledge Dr. B. Boudjelida, for providing access to a Dimension FastScan Atomic Force Microscope at BRUKER's headquarter's, Coventry, UK and Dr. Robert Ranson for providing training on the Nd:YAG laser used for this work.

## References

- [1] S.A. Maier, *Plasmonics: Fundamentals and Applications*, Springer, New York, 2007.
- [2] U. Kreibitz, M. Vollmer, *Optical Properties of Metal Clusters*, Springer, Berlin, 1995.
- [3] K.A. Willets, R.P. Van Duyne, Localized surface plasmon resonance spectroscopy and sensing, *Annu. Rev. Phys. Chem.* 58 (2007) 267.
- [4] G.V. Hartland, Optical studies of dynamics in noble metal nanostructures, *Chem. Rev.* 111 (2011) 3858.
- [5] M.R. Jones, K.D. Osberg, R.J. Macfarlane, M.R. Langille, C.A. Mirkin, Templated techniques for the synthesis and assembly of plasmonic nanostructures, *Chem. Rev.* 111 (2011) 3736.
- [6] X. Lu, M. Rycenga, S.E. Skrabalak, B.J. Wiley, Y. Xia, Chemical synthesis of novel plasmonic nanoparticles, *Annu. Rev. Phys. Chem.* 60 (2009) 167.
- [7] N.J. Halas, Plasmonics: an emerging field fostered by Nano Letters, *Nano Lett.* 10 (2010) 3816.
- [8] M.L. Brongersma, V.M. Shalaev, The case for plasmonics, *Science* 328 (2010) 440.
- [9] J.A. Fan, C. Wu, K. Bao, J. Bao, R. Bardhan, N.J. Halas, V.N. Manoharan, P. Nordlander, G. Shvets, F. Capasso, Self-assembled plasmonic nanoparticle clusters, *Science* 328 (2010) 1135.
- [10] E. Ozbay, Plasmonics: merging photonics and electronics at nanoscale dimensions, *Science* 311 (2006) 189.
- [11] E. Lidorikis, Modeling of enhanced absorption and Raman scattering caused by plasmonic nanoparticle near fields, *J. Quant. Spectrosc. Radiat. Transf.* 113 (2012) 2573.
- [12] C.F. Bohren, D.R. Huffman, *Absorption and Scattering of Light by Small Particles*, Wiley, New York, 1983.
- [13] A.J. Haes, C.L. Haynes, A.D. McFarland, G.C. Schatz, R.P. Van Duyne, S.L. Zou, Plasmonic materials for surface-enhanced sensing and spectroscopy, *MRS Bull.* 30 (2005) 368.
- [14] K.S. Lee, M.A.J. El-Sayed, Gold and silver nanoparticles in sensing and imaging: sensitivity of plasmon response to size, shape and metal composition, *J. Phys. Chem. B* 110 (2006) 19220.
- [15] M.M. Miller, A.A. Lazarides, Sensitivity of metal nanoparticle surface plasmon resonance to the dielectric environment, *J. Phys. Chem. B* 109 (2005) 21556.
- [16] O. Kvitck, J. Siegel, V. Hnatowicz, V. Svorcik, Noble metal nanostructures: influence of structure and environment on their optical properties, *J. Nanomater.* (2013) (Art. No 743684).
- [17] N.J. Halas, Playing with plasmons: tuning the optical resonant properties of metallic nanoshells, *MRS Bull.* 30 (2005) 362.
- [18] S. Underwood, P. Mulvaney, Effect of solution refractive index on the color of gold colloids, *Langmuir* 10 (1994) 3427.
- [19] J.J. Mock, M. Barbic, D.R. Smith, D.A. Schultz, S.J. Schultz, Shape effects in plasmon resonance of individual colloidal silver nanoparticles, *J. Chem. Phys.* 116 (2002) 6755.
- [20] G. Walters, I.P. Parkin, The incorporation of noble metal nanoparticles into host matrix thin films: synthesis, characterisation and applications, *J. Mater. Chem.* 19 (2009) 574.
- [21] M. Rycenga, C.M. Cobley, J. Zeng, W. Li, C.H. Moran, Q. Zhang, D. Qin, Y. Xia, Controlling the synthesis and assembly of silver nanostructures for plasmonic applications, *Chem. Rev.* 111 (2011) 3669.
- [22] L. Armelao, D. Barreca, G. Bottaro, A. Gasparotto, S. Gross, C. Maragnob, E. Tondello, Recent trends on nanocomposites based on Cu, Ag and Au clusters: a closer look, *Coord. Chem. Rev.* 250 (2006) 1294.
- [23] M.B. Cortie, A.M. McDonagh, Synthesis and optical properties of hybrid and alloy plasmonic nanoparticles, *Chem. Rev.* 111 (2011) 3713.
- [24] J.N. Anker, W.P. Hall, O. Lyandres, N.C. Shah, J. Zhao, R.P. Van Duyne, Biosensing with plasmonic nanosensors, *Nat. Mater.* 7 (2008) 442.
- [25] K.M. Mayer, J.H. Hafner, Localized surface plasmon resonance sensors, *Chem. Rev.* 111 (2011) 3828.
- [26] Y. Jin, Engineering plasmonic gold nanostructures and metamaterials for biosensing and nanomedicine, *Adv. Mater.* 24 (2012) 5153.
- [27] E. Usukura, S. Shinohara, K. Okamoto, J. Lim, K. Char, K. Tamada, Highly confined enhanced surface fluorescence imaging with two-dimensional silver nanoparticle sheets, *Appl. Phys. Lett.* 104 (2014) (Art. No 121906).
- [28] M. Moskovits, Surface-enhanced spectroscopy, *Rev. Mod. Phys.* 57 (1985) 783.
- [29] K. Kneipp, Y. Wang, H. Kneipp, L.T. Perelman, I. Itzkan, R.R. Dasari, M.S. Feld, Single molecule detection using surface-enhanced Raman scattering (SERS), *Phys. Rev. Lett.* 78 (9) (1997) 1667.
- [30] Y. Fang, N.H. Seong, D.D. Dlott, Measurement of the distribution of site enhancements in surface-enhanced Raman scattering, *Science* 321 (2008) 388.
- [31] S.J. Henley, J.D. Carey, S.R.P. Silva, Laser-nanostructured Ag films as substrates for surface-enhanced Raman spectroscopy, *Appl. Phys. Lett.* 88 (2006) (Art. No 081904).
- [32] S.J. Henley, S.R.P. Silva, Laser direct write of silver nanoparticles from solution onto glass substrates for surface-enhanced Raman spectroscopy, *Appl. Phys. Lett.* 91 (2007) (Art. No 023107).
- [33] M.L. de la Chapelle, P.G. Gucciardi, N. Lidgi-Guigui (Eds.), *Handbook of Enhanced Spectroscopy*, Pan Stanford, 2015.
- [34] C.H. Lin, L. Jiang, J. Zhou, H. Xiao, S.J. Chen, H.L. Tsai, Laser-treated substrate with nanoparticles for surface-enhanced Raman scattering, *Opt. Lett.* 35 (7) (2010) 941.
- [35] D. Wan, H.L. Chen, S.C. Tseng, L.A. Wang, Y.P. Chen, One-shot deep-UV pulsed-laser-induced photomodification of hollow metal nanoparticles for high-density data storage on flexible substrates, *ACS Nano* 4 (2010) 165.
- [36] P. Zijlstra, J.W.M. Chon, M. Gu, Five-dimensional optical recording mediated by surface plasmons in gold nanorods, *Nature* 459 (2009) 410.
- [37] C. Ryan, C.W. Christenson, B. Valle, A. Saini, J. Lott, J. Johnson, D. Schiraldi, C. Weder, E. Baer, K.D. Singer, J. Shan, Roll-to-roll fabrication of multilayer films for high capacity optical data storage, *Adv. Mater.* 24 (2012) 5222.
- [38] W.T. Chen, P.C. Wu, C.J. Chen, C.J. Weng, H.C. Lee, T.J. Yen, C.H. Kuan, M. Mansuripur, D.P. Tsai, Manipulation of multidimensional plasmonic spectra for information storage, *Appl. Phys. Lett.* 98 (2011) (Art. No 171106).
- [39] N. Lagos, M.M. Sigalas, E. Lidorikis, Theory of plasmonic near-field enhanced absorption in solar cells, *Appl. Phys. Lett.* 99 (2011) (Art. No 063304).
- [40] N. Kalfagiannis, P.G. Karagiannidis, C. Pitsalidis, N.T. Panagiotopoulos, C. Gravalidis, S. Kassavetis, P. Patsalas, S. Logothetidis, Plasmonic silver nanoparticles for improved organic solar cells, *Sol. Energy Mater. Sol. Cells* 104 (2012) 165.
- [41] H.A. Atwater, A. Polman, Plasmonics for improved photovoltaic devices, *Nat. Mater.* 9 (2010) 205.
- [42] M.J. Beliatis, S.J. Henley, S. Han, K. Gandhi, A.A.D.T. Adikaari, E. Stratakis, E. Kymakis, S.R.P. Silva, Organic solar cells with plasmonic layers formed by laser nanofabrication, *Phys. Chem. Chem. Phys.* 15 (2013) 8237.
- [43] H. Zoubos, L.E. Koutsokeras, D.F. Anagnostopoulos, E. Lidorikis, S.A. Kalogirou, A.R. Wildes, P.C. Kelires, P. Patsalas, Broadband optical absorption of amorphous carbon/Ag nanocomposite films and its potential for solar harvesting applications, *Sol. Energy Mater. Sol. Cells* 117 (2013) 350.
- [44] P. Nikolau, C. Mina, M. Constantinou, L.E. Koutsokeras, G. Constantinides, E. Lidorikis, A. Avgeropoulos, P.C. Kelires, P. Patsalas, Functionally graded poly(dimethylsiloxane)/silver nanocomposites with tailored broadband optical absorption, *Thin Solid Films* 581 (2015) 14.
- [45] J.R. Cole, N.J. Halas, Optimized plasmonic nanoparticle distributions for solar spectrum harvesting, *Appl. Phys. Lett.* 89 (2006) (Art. No 153120).
- [46] G. Kakavelakis, I. Vangelidis, A. Heuer-Jungemann, A.G. Kanaras, E. Lidorikis, E. Stratakis, E. Kymakis, Plasmonic backscattering effect in high-efficient organic photovoltaic devices, *Adv. Energy Mater.* 6 (2016) (Art. No 1501640).
- [47] A. Siozios, N. Kalfagiannis, D.V. Bellas, C. Bazioti, G.P. Dimitrakopoulos, G. Vourlias, W.M. Cranton, E. Lidorikis, D.C. Koutsogeorgis, P. Patsalas, Sub-surface laser nanostructuring in stratified metal/dielectric media: a versatile platform towards flexible, durable and large-scale plasmonic writing, *Nanotechnology* 26 (2015) (Art. No 155301).
- [48] C. Bazioti, G.P. Dimitrakopoulos, T. Kehagias, P. Komninou, A. Siozios, E. Lidorikis, D.C. Koutsogeorgis, P. Patsalas, Influence of laser annealing on the structural properties of sputtered AlN:Ag plasmonic nanocomposites, *J. Mater. Sci.* 49 (2014) 3996.
- [49] A. Siozios, D.C. Koutsogeorgis, E. Lidorikis, G.P. Dimitrakopoulos, T. Kehagias, H. Zoubos, P. Komninou, W.M. Cranton, C. Kosmidis, P. Patsalas, Optical encoding by plasmon-based patterning: hard and inorganic materials become photosensitive, *Nano Lett.* 12 (2012) 259.
- [50] A. Siozios, D.C. Koutsogeorgis, E. Lidorikis, G.P. Dimitrakopoulos, N. Pliatsikas, G. Vourlias, T. Kehagias, P. Komninou, W. Cranton, C. Kosmidis, P. Patsalas, Laser-matter interactions, phase changes and diffusion phenomena during laser annealing of plasmonic AlN:Ag templates and their applications in optical encoding, *J. Phys. D: Appl. Phys.* 48 (2015) (Art. No 285306).
- [51] M. Torrell, P. Machado, L. Cunha, N.M. Figueiredo, J.C. Oliveira, C. Louro, F. Vaz, Development of new decorative coatings based on gold nanoparticles dispersed in an amorphous TiO<sub>2</sub> dielectric matrix, *Surf. Coat. Technol.* 204 (2010) 1569.
- [52] J. Henson, J.C. Heckel, E. Dimakis, J. Abell, A. Bhattacharyya, G. Chumanov, T.D. Moustakas, R. Paiella, Plasmon enhanced light emission from InGaN quantum wells via coupling to chemically synthesized silver nanoparticles, *Appl. Phys. Lett.* 95 (2009) (Art. No 151109).
- [53] J.H. Seo, J.H. Park, S.I. Kim, B.J. Park, Z. Ma, J. Choi, B.K. Ju, Nanopatterning by laser interference lithography: applications to optical devices, *J. Nanosci. Nanotechnol.* 14 (2014) 1521.
- [54] U. Guler, J.C. Ndukaife, G.V. Naik, A.G.A. Nnanna, A.V. Kildishev, V.M. Shalaev, A. Boltasseva, Local heating with lithographically fabricated plasmonic titanium nitride nanoparticles, *Nano Lett.* 13 (2013) 6078.
- [55] G. Bracher, K. Schraml, M. Ossianer, S. Fr ed eric, J.J. Finley, M. Kaniber, Optical study of lithographically defined, subwavelength plasmonic wires and their coupling to embedded quantum emitters, *Nanotechnology* 25 (2014) (Art. No 075203).
- [56] J. Toudert, D. Babonneau, S. Camello, T. Girardeau, F. Yubero, J.P. Espin os, A.R. Gonzalez-Elipe, Using ion beams to tune the nanostructure and optical response of co-deposited Ag:BN thin films, *J. Phys. D: Appl. Phys.* 40 (2007) 4614.
- [57] V.A. Sivakov, K. H oflich, M. Becker, A. Berger, T. Stelzner, K.E. Elers, V. Pore, M. Ritala, S.H. Christiansen, Silver coated platinum core-shell nanostructures on etched Si nanowires: atomic layer deposition (ALD) processing and application in SERS, *Chem. Phys. Chem.* 11 (2010) 1995.
- [58] Y. Lu, J.Y. Huang, C. Wang, S. Sun, J. Lou, Cold welding of ultrathin gold nanowires, *Nat. Nanotechnol.* 5 (2010) 218.
- [59] Y.K. Mishra, S. Mohapatra, D. Kabiraj, B. Mohanta, N.P. Lalla, J.C. Pivin, D.K. Avasthi, Synthesis and characterization of Ag nanoparticles in silica matrix by atom beam sputtering, *Scr. Mater.* 56 (2007) 629.
- [60] I. Tanahashi, Y. Manabe, T. Tohda, S. Sasaki, A. Nakamura, Optical nonlinearities of Au/SiO<sub>2</sub> composite thin films prepared by a sputtering method, *J. Appl. Phys.* 79 (1996) 1244.
- [61] D. Lin, H. Tao, J. Trevino, J.P. Mondia, D.L. Kaplan, F.G. Omenetto, L. Dal Negro, Direct transfer of subwavelength plasmonic nanostructures on bioactive silk films, *Adv. Mater.* 24 (2012) 6088.
- [62] P. Nielsen, P. Morgen, A.C. Simonsen, O. Albrektsen, Hemispherical shell nanostructures from metal-stripped embossed alumina on aluminum templates, *J. Phys. Chem. C* 115 (2011) 5552.
- [63] J.H. Park, P. Nagpal, K.M. McPeak, N.C. Lindquist, S.H. Oh, D.J. Norris, Fabrication of smooth patterned structures of refractory metals, semiconductors, and oxides via template stripping, *Appl. Mater. Interfaces* 5 (2013) 9701.
- [64] P. Farzinpour, A. Sundar, K.D. Gilroy, Z.E. Eskin, R.A. Hughes, S. Neretina, Dynamic templating: a large area processing route for the assembly of periodic arrays of sub-micrometer and nanoscale structures, *Nanoscale* 5 (2013) 1929.

- [65] N. Kalfagiannis, A. Siozios, D.V. Bellas, D. Toliopoulos, L. Bowen, N. Pliatsikas, W.M. Cranton, C. Kosmidis, D.C. Koutsogeorgis, E. Lidorikis, P. Patsalas, Selective modification of nanoparticle arrays by laser-induced self assembly (MONA-LISA): putting control into bottom-up plasmonic nanostructuring, *Nanoscale* 8 (2016) 8236.
- [66] S.J. Henley, J.D. Carey, S.R.P. Silva, Pulsed-laser-induced nanoscale island formation in thin metal-on-oxide films, *Phys. Rev. B* 72 (2005) (Art. No 195408).
- [67] M.J. Beliatis, S.J. Henley, S.R.P. Silva, Engineering the plasmon resonance of large area bimetallic nanoparticle films by laser nanostructuring for chemical sensors, *Opt. Lett.* 36 (8) (2011) 1362.
- [68] K. Christou, I. Knorr, J. Ihlemann, H. Wackerbarth, V. Beushausen, Fabrication and characterization of homogeneous surface-enhanced Raman scattering substrates by single pulse UV-laser treatment of gold and silver films, *Langmuir* 26 (23) (2010) 18564.
- [69] C. Favazza, R. Kalyanaraman, R. Sureshkumar, Robust nanopatterning by laser-induced dewetting of metal nanofilms, *Nanotechnology* 17 (2006) 4229.
- [70] H. Krishna, N. Shirato, C. Favazza, R. Kalyanaraman, Pulsed laser induced self-organization by dewetting of metallic films, *J. Mater. Res.* 26 (2) (2011) 154.
- [71] C.E. Rodríguez, R.J. Peláez, C.N. Afonso, S. Riedelb, P. Leidererb, D. Jimenez-Reyc, A. Climent-Fontc, Plasmonic response and transformation mechanism upon single laser exposure of metal discontinuous films, *Appl. Surf. Sci.* 302 (2014) 32.
- [72] F. Ruffino, A. Pugliara, E. Carria, C. Bongiorno, C. Spinella, M.G. Grimaldi, Formation of nanoparticles from laser irradiated Au thin film on SiO<sub>2</sub>/Si: elucidating the Rayleigh-instability role, *Mater. Lett.* 84 (2012) 27.
- [73] F. Ruffino, E. Carria, S. Kimiagar, I. Crupi, F. Simone, M.G. Grimaldi, Formation and evolution of nanoscale metal structures on ITO surface by nanosecond laser irradiations of thin Au and Ag films, *Sci. Adv. Mater.* 4 (2012) 708.
- [74] F. Ruffino, A. Pugliara, E. Carria, L. Romano, C. Bongiorno, G. Fiscaro, A. La Magna, C. Spinella, M.G. Grimaldi, Towards a laser fluence dependent nanostructuring of thin Au films on Si by nanosecond laser irradiation, *Appl. Surf. Sci.* 258 (2012) 9128.
- [75] S.J. Henley, C.H.P. Poa, A.A.D.T. Adikaari, C.E. Giusca, J.D. Carey, S.R.P. Silva, Excimer laser nanostructuring of nickel thin films for the catalytic growth of carbon nanotubes, *Appl. Phys. Lett.* 84 (2004) (Art. No 4035).
- [76] S.J. Henley, J.D. Carey, S.R.P. Silva, Metal nanoparticle production by pulsed laser nanostructuring of thin metal films, *Appl. Surf. Sci.* 253 (2007) 8080.
- [77] J. Trice, D. Thomas, C. Favazza, R. Sureshkumar, R. Kalyanaraman, Pulsed-laser-induced dewetting in nanoscopic metal films: theory and experiments, *Phys. Rev. B* 75 (2007) (Art. No 235439).
- [78] E.D. Palik, *Handbook of Optical Constants of Solids*, Academic, San Diego, 1998.
- [79] The optical properties of AlN where taken after ellipsometric measurements in our laboratory.
- [80] D.E. Aspens, Optical properties of thin films, *Thin Solid Films* 89 (1982) 249.
- [81] J.E. Spanier, I.P. Herman, Use of hybrid phenomenological and statistical effective-medium theories of dielectric functions to model the infrared reflectance of porous SiC films, *Phys. Rev. B* 61 (2000) 10437.
- [82] E. Simsek, Effective refractive index approximation and surface plasmon resonance modes of metal nanoparticle chains and arrays, *PIERS* 5 (7) (2009) 629.
- [83] O. Deparis, Poynting vector in transfer-matrix formalism for the calculation of light absorption profile in stratified isotropic optical media, *Opt. Lett.* 36 (20) (2011) 3960.
- [84] J.D. Jackson, *Classical Electrodynamics*, Wiley, New York, 1999.
- [85] A. Taflove, S.C. Hagness, *Computational Electrodynamics: the Finite-Difference Time-Domain Method*, third ed. Artech House, Boston, 2005.
- [86] E. Lidorikis, S. Egusa, J.D. Joannopoulos, Effective medium properties and photonic crystal superstructures of metallic nanoparticle arrays, *J. Appl. Phys.* 101 (2007) (Art. No 054304).
- [87] F. Schedin, E. Lidorikis, A. Lombardo, V.G. Kravets, A.K. Geim, A.N. Grigorenko, K.S. Novoselof, A.C. Ferrari, Surface-enhanced Raman spectroscopy of graphene, *ACS Nano* 4 (2010) 5617.
- [88] E. Lidorikis, A.C. Ferrari, Photonics with multiwall carbon nanotube arrays, *ACS Nano* 3 (2009) 1238.
- [89] D.R. Lide, *CRC Handbook of Chemistry and Physics*, 85th ed. CRC Press, Boca Raton, FL, 2005.
- [90] S.R. Choi, D. Kim, S.H. Cho, S.H. Lee, J.K. Kim, Thermal conductivity of AlN and SiC thin films, *Int. J. Thermophys.* 27 (2006) 896.
- [91] C. Duquenne, M.P. Besland, P.Y. Tessier, E. Gautron, Y. Scudeller, D. Averty, Thermal conductivity of aluminium nitride thin films prepared by reactive magnetron sputtering, *J. Phys. D. Appl. Phys.* 45 (2012) 015301.
- [92] G.A. Slack, R.A. Tanzilli, R.O. Pohl, J.W. Vandersande, The intrinsic thermal conductivity of AlN, *J. Phys. Chem. Solids* 48 (1987) 641.
- [93] J.R. Welty, C.E. Wicks, R.E. Wilson, G.L. Rorrer, *Fundamentals of Momentum, Heat, and Mass Transfer*, Wiley, New York, 2008.
- [94] P.K. Jain, W. Huang, M.A. El-Sayed, On the universal scaling behavior of the distance decay of plasmon coupling in metal nanoparticle pairs: a plasmon ruler equation, *Nano Lett.* 7 (2007) 2080.
- [95] P.H. Klein, W.J. Croft, Thermal conductivity, diffusivity, and expansion of Y2O3, Y3Al5O12, and LaF3 in the range 77–300 K, *J. Appl. Phys.* 38 (1967) 1603.
- [96] Y. Nishijima, L. Rosa, S. Juodkakis, Surface plasmon resonances in periodic and random patterns of gold nano-disks for broadband light harvesting, *Opt. Express* 2010 (2012) 11466.
- [97] F. Hubenthal, Nanoparticles and their tailoring with laser light, *Eur. J. Phys.* 30 (2009) S49.